

See discussions, stats, and author profiles for this publication at:
<https://www.researchgate.net/publication/228030340>

In-situ X-ray Diffraction Studies of the Electrode/Solution Interface

CHAPTER · MARCH 2008

DOI: 10.1002/9783527616817.ch1

READS

10

2 AUTHORS:



Christopher A Lucas

University of Liverpool

27 PUBLICATIONS 2,582 CITATIONS

SEE PROFILE



N. M. Marković

Argonne National Laboratory

284 PUBLICATIONS 21,298 CITATIONS

SEE PROFILE

1

**In-situ X-ray Diffraction Studies
of the Electrode/Solution Interface**

Christopher A. Lucas and Nenad M. Marković

1.1

Introduction

Since the early days of modern surface science, the main goal in the electrochemical community has been to find correlations between the microscopic structures formed by surface atoms and adsorbates and the macroscopic kinetic rates of a particular electrochemical reaction. The establishment of such relationships, previously only developed for catalysts under ultrahigh vacuum (UHV) conditions, has been broadened to embrace electrochemical interfaces. In early work, determination of the surface structures in an electrochemical environment was derived from *ex-situ* UHV analysis of emersed surfaces. Although such *ex-situ* tactics remain important, the relationship between the structure of the interface in the electrolyte and that observed in UHV was always problematic and had to be carefully examined on a case-by-case basis. The application of *in-situ* surface-sensitive probes, most notably synchrotron-based surface X-ray scattering (SXS) [1–6] and scanning tunneling microscopy (STM) [7, 8], has overcome this “emersion gap” and provided information on potential-dependent surface structures at a level of sophistication that is on a par with (or even in advance of) that obtained for surfaces in UHV.

In this chapter, we review some applications of the SXS technique for exploring surface atomic structure in an electrochemical environment. While the choice of topics is extracted mainly from recent studies, the survey will provide a full perspective into the potential value of SXS for exploiting many fundamental issues pertaining to the development of surface electrochemistry as a science. SXS is an ideal technique for probing, in detail, the surface atomic structure, and such structural details can be important in understanding some electrochemical systems. In this article, however, we highlight the use of SXS in potentiodynamic measurements where the aim is to correlate directly the electrochemical reactivity with atomic-scale structural changes at the electrode surface. The review begins with a description of the potential/adsorbate-induced changes in a metal surface, focusing on those cases where detailed and rather complete surface coverages and/or structures have been determined. Central to the adsorbate-induced changes in

monometallic (Pt metals and IB group metals) and some of their bimetallic single-crystal surfaces are the concepts of relaxation and reconstruction of near-surface atoms. The data for adsorbate-induced restructuring effects on Pt and Au single-crystal surfaces far outnumber those for Ag, Cu, and bimetallic surfaces; the references in this chapter, however, show them side by side for comparison. The next section describes the atomic/molecular scale structures of adsorbed anions and cations on single-crystal surfaces and summarizes applications of the SXS technique for exploring the behavior of molecules in the temperature range which is important for the development of the polymer electrolyte fuel cell. Most of adsorbate surface structures are indicated in the text, so that they can be directly related to the nature of the substrate and the supporting electrolytes. The review concludes with some examples of how SXS can be utilized for elucidating the structure changes at the metal-oxide/electrolyte interface.

1.2

Experimental

Surface X-ray diffraction is now a well-established technique for probing the atomic structure at the electrochemical interface, and, since the first *in-situ* synchrotron X-ray study in 1988 [1], several groups have used the technique to probe a variety of electrochemical systems [1, 2, 9]. It is beyond the scope of this article to provide a comprehensive description of basic X-ray diffraction from surfaces. Readers are referred to the excellent reviews by Feidenhans'l [10], Fuoss and Brennan [11], and Robinson and Tweet [12] for explicit details. It should be noted that, throughout this review, the acronym SXS is used to describe the X-ray measurements, although all of the results are obtained by X-ray diffraction.

The majority of the results presented in this report are X-ray diffraction studies of the three low-index surfaces of metal crystals with the face-centered cubic (*fcc*) crystal structure. The close-packed (111) surface has a hexagonal unit cell that is defined such that the surface normal is along the $(0, 0, l)_{\text{hex}}$ direction and the $(h, 0, 0)_{\text{hex}}$ and $(0, k, 0)_{\text{hex}}$ vectors lie in the plane of the surface and subtend 60° . The units for h , k and l are $a^* = b^* = 4\pi/\sqrt{3a_{\text{NN}}}$ and $c^* = 2\pi/\sqrt{6a_{\text{NN}}}$ where a_{NN} is the nearest-neighbor distance in the crystal. Because of the stacking of the ABC along the surface normal direction, the unit cell contains three monolayers, and the Bragg reflections are spaced apart by multiples of three in l . The (001) surface is more open than the (111) surface and is indexed to a surface tetragonal unit cell. This is related to the conventional cubic unit cell by the transformations $(1, 0, 0)_t = 1/2(2, 2, 0)_c$, $(0, 1, 0)_t = 1/2(2, -2, 0)_c$ and $(0, 0, 1)_t = (0, 0, 1)_c$. The units for h , k and l are $a^* = b^* = 2\pi/a_{\text{NN}}$ and $c^* = 4\pi/\sqrt{2a_{\text{NN}}}$. Finally, the (110) reciprocal surface unit cell is rectangular and the reciprocal lattice notation is such that h is along $[1 \ -1 \ 0]$, k along $[0 \ 0 \ 1]$ and l is along the $[1 \ 1 \ 0]$ surface normal. The units for h , k and l are $a^* = c^* = 2\pi/a_{\text{NN}}$ and $b^* = 4\pi/\sqrt{2a_{\text{NN}}}$.

As in the UHV environment [13], the extraction of structural information, such as surface coverage, surface roughness and layer spacings (both adsorbate-

substrate distances and the expansion/contraction of the substrate surface atoms themselves) at the electrified solid/liquid interface relies on measurement of the crystal truncation rods (CTRs). By combining specular CTR results (where the momentum transfer, \mathbf{Q} , is entirely along the surface normal direction) with non-specular CTR results (where \mathbf{Q} has an additional in-plane contribution) it is possible to build up a 3-dimensional picture of the atomic structure at the electrode surface. If the surface or adlayer adopts a different symmetry from that of the underlying bulk crystal lattice, then the scattering from the surface becomes separate from that of the bulk in reciprocal space and it is possible to measure the surface scattering independently. This independent structural information can be combined with CTR analysis to give the registry of the surface layers with respect to the bulk lattice [10, 11, 13].

Apart from the standard analysis of CTR data, perhaps the most interesting application of SXS is in potentiodynamic measurements, i.e. when the scattered X-ray intensity is measured at a particular reciprocal lattice position as the electrode potential is cycled over a given range. We have termed this technique X-ray voltammetry (XRV), although a few alternative terms have been used in the literature. By measuring the XRV at a number of different CTR positions, an insight into the nature of the structural changes at the surface can be obtained without recourse to the detailed measurement of the CTR profiles [14, 15]. If scattering due to an ordered surface layer with a different symmetry to that of the underlying bulk crystal is obtained, then measurement of the potential dependence of this scattering directly indicates the potential range of stability of the structure. This information is particularly useful for comparison with cyclic voltammetry (CV) results, as features in the CV can be directly correlated with structural changes at the electrode surface.

A key aspect in the study of single-crystal metal electrodes is the preparation of the surface prior to the experiment and the transfer of the crystal into the electrochemical X-ray cell. One approach is to prepare the surface in a UHV environment by cycles of ion sputtering and annealing. This methodology has the advantage that the surface quality can be checked during preparation by standard surface science techniques such as LEED and Auger Electron Spectroscopy. UHV preparation is important for bimetallic surfaces for which precise surface compositions are dependent on annealing temperatures. An alternative method for surface preparation for some crystals is to use the flame-annealing technique [16–18]. After pretreatment to produce a flat, well-oriented surface, the crystal is heated in a hydrogen or butane flame and then allowed to cool in air or hydrogen/argon before transfer to the electrochemical X-ray cell. This procedure has been used successfully for the preparation of Au(*hkl*) and Pt(*hkl*) surfaces. Other monometallic metal surfaces, such as Cu and Ni, cannot be prepared by flame-annealing methods. Other than UHV preparation, the most successful method for these surfaces, including Ag, has been to use a long pre-anneal of the surface in a forming gas, such as hydrogen, followed by a short electrochemical etch, rinsing with water, and then direct transfer into the electrochemical X-ray cell [19–21].

1.3

Adsorbate-induced Restructuring of Metal Substrates

Modern surface crystallographic studies have shown that on the atomic scale most clean metals tend to minimize their surface energy by two kinds of surface atom rearrangements, *relaxation* and *reconstruction*, which collectively may be called *restructuring*. Relaxation of metal surfaces is usually defined as small interlayer spacing changes relative to the ideal bulk lattice [22–26]. The displacements should be small compared to near-neighbor distances, such that no bond-breaking/bond-making events take place within the substrate. Adsorbate-induced relaxations occur in many varieties: as *interlayer spacing changes*, where the top layer of metal atoms undergo inward or outward relaxation; *lateral relaxation*, in which surface atoms are shifted parallel to the surface (for example, adsorbate-induced collective rotation of substrate atoms around an adsorbate site), and *layer buckling*, whereby a coplanar atomic layer loses its coplanarity because of preferred adsorption on a particular surface site. Reconstruction, on the other hand, involves large atomic displacements both perpendicular to and parallel to the surface plane leading to re-bonding and a change in the periodicity of the surface with respect to the underlying substrate. The periodicity of the surface can be defined by Woods' notation; for example an unreconstructed Pt(110) surface would be termed as (1×1) whereas if the surface unit cell size was doubled in one of the primary vector directions it would be termed as (2×1) etc.

The present knowledge of surface restructuring at electrified metal/solution interfaces would not have been possible without certain key advances, for example, the many excellent UHV [24] and theoretical studies [27], which will not be reviewed in this article. A further advance was the advent of *in-situ* surface-sensitive techniques and the development of efficient methods for surface preparation of monometallic and bimetallic single-crystal surfaces and their clean transfer from UHV into the electrochemical environment [28, 29]. Within the framework of this article, it would be impossible to provide a comprehensive review of these experiments. For these reasons, the surface reconstruction and relaxation of monometallic Pt(*hkl*) and Au(*hkl*) single-crystal surfaces, induced by the adsorption of hydrogen¹⁾ ($\text{H}^+ + \text{e}^- = \text{H}_{\text{upd}}$ in acid electrolytes and $\text{H}_2\text{O} + \text{e}^- = \text{H}_{\text{upd}} + \text{OH}^-$ in alkaline solutions) and oxygenated species²⁾ ($\text{H}_2\text{O} = \text{OH}_{\text{ad}} + \text{H}^+ + \text{e}^-$ in acid solution and $\text{OH}^- = \text{OH}_{\text{ad}} + \text{e}^-$ in alkaline solution), are not discussed in great detail. In preference, the focus is on systems of catalytic interest, i.e., hydrogen- and oxygen-in-

1) In electrochemistry, adsorbed hydrogen is denoted as either the underpotentially deposited hydrogen, H_{upd} , that is the H adlayer formed under thermodynamic equilibrium conditions where the coverage is changed reversibly with the potential applied or the overpotentially deposited hydrogen, H_{opd} , as defined by Conway and co-workers [102] for the

hydrogen evolution reaction, i.e.
 $2\text{H}^+ + 2\text{e}^- = \text{H}_2$.

2) Two different types of chemisorbed oxygen-containing species are proposed to form on *fcc* metals, a reversible form (denoted hereafter as OH_{ad}) and an irreversible form, which we shall call "oxide" hereafter.

duced restructuring of bimetallic surfaces as well as CO-induced changes in the surface structure of Pt(*hkl*), Au(*hkl*), and their bimetallic alloys.

1.3.1

Surface Relaxation

There have been numerous experimental and theoretical studies of the relaxation of metal surfaces in UHV, and a significant data base now exists based mainly on LEED studies. In UHV, on unreconstructed clean low-index single-crystal surfaces it is often found that the outermost layer of atoms is *contracted* toward the second atomic layer. The tendency for surface contraction has been explained by Finnis and Heine using the Hellman-Feynman theorem, which states that the force on an ion is just the electrostatic force from the other ions and the self-consistent electron density. Adsorption onto clean metal surfaces in UHV often reverses the surface contraction such that the outermost layer of atoms is *expanded* away from the second atomic layer. These concepts can be extended to the metal/electrolyte interface, and, indeed, surface relaxation has been observed at coinage-metal surfaces (Cu, Ag, Au) as well as at Pt-group monometallic and bimetallic single-crystal surfaces in the electrochemical environment. Key results are presented below with the aim of providing a suitable framework for the discussion of adsorbate-induced interlayer spacing changes, lateral relaxation, and layer buckling.

1.3.1.1 Pt Monometallic and Bimetallic Surfaces

The restructuring of Pt single-crystal surfaces has previously been described in some detail [28, 29], and so in this section new results for adsorbate-induced restructuring of Pt bimetallic surfaces are presented. Two types of bimetallic surfaces will be used as model systems: the surface of a Pt₃Sn(111) bulk alloy crystal and ultra thin metal films of Pd deposited onto Pt(111) and Pt(100), hereafter denoted as Pt(*hkl*)-Pd_x (0 < x < 4 ML) systems. Key to the success of these experiments is the fact that both the UHV-prepared p(2×2) structure of Pt₃Sn(111) [30, 31] as well as electrochemically- or UHV-prepared thin films of Pd on Pt(*hkl*) [32–34] can be transferred into an electrochemical SXS cell without altering the surface structure and composition. The surfaces are also stable between the potential for the hydrogen evolution reaction and that for reversible oxide formation, indicating that the energy of adsorption of H_{upd}, OH_{ad}, and anions is not strong enough to induce surface reconstruction.

As noted in Section 1.2, accurate determination of adsorbate-induced changes in surface-normal structure, i.e. the Δd_{12} interplanar spacing between the first and the second atomic layers, can be achieved by measuring the CTRs [1–4, 10, 35]. Previous reviews summarized adsorbate-induced relaxation and reconstruction on well-defined Pt(*hkl*) and Pt–bimetallic surfaces in aqueous electrolytes at electrode potentials at which a maximum surface coverage of adsorbed species is established [28, 29]. The data revealed that either close to the hydrogen evolu-

tion potential (0.05 V) or close to the onset of irreversible oxide formation (ca. 1 V) the surface expansion increases in the sequence $\text{Pt}(111) < \text{Pt}(100) < \text{Pt}(110)$ in both H_2SO_4 and KOH solutions. It has been proposed that the observed differences in relaxation of $\text{Pt}(hkl)$ arise because of the interplay between the Pt-adsorbate bonding and the coordination of surface atoms (for details see [28]).

Direct confirmation of the relationship between surface relaxation and binding interaction is obtained in experiments in which relatively weakly bonded H_{upd} is displaced from the surface by strongly bonded CO. As shown previously [28], following the adsorption of CO onto $\text{Pt}(111)$ at 0.05 V, the surface expansion increases from 2% on the H_{upd} -covered surface to 4% on the CO-covered surface, supporting the proposition that the difference in relaxation can be correlated with metal-adsorbate bonding, the Pt-CO interaction being much stronger than the Pt- H_{upd} interaction. The surface coverage by CO at 0.05 V is 0.75 ML and a $\text{p}(2 \times 2)\text{-3CO}$ structure is formed that can be measured by SXS [ML=amount of monolayer adsorption]. As will be discussed in Section 1.4, the potential stability of the $\text{p}(2 \times 2)\text{-3CO}$ structure is strongly affected by the oxidation of a small fraction of the CO adlayer, so that at 0.65 V a $(\sqrt{19} \times \sqrt{19})\text{-13 CO}$ structure (hereafter dubbed the “ $\sqrt{19}$ ” structure) forms with $\theta_{\text{CO}} = 0.68$ ML. Very recently, the structural relaxation of the $\text{Pt}(111)\text{-CO}$ surface has been studied in detail in the presence of the “ $\sqrt{19}$ ” structure [36]. The structural model of the $\text{Pt}(111)$ surface relaxation induced by the “ $\sqrt{19}$ ” phase in Fig. 1.1 shows that different layer expansions and in-plane rotations occur for the Pt atoms un-

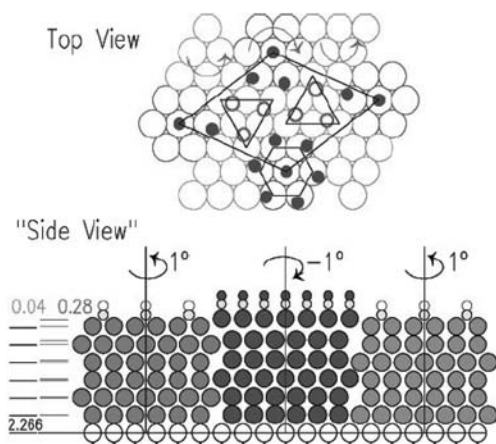


Fig. 1.1 Structural model of the $\text{Pt}(111)$ surface relaxation in 0.1 M HClO_4 induced by the $(\sqrt{19} \times \sqrt{19})\text{-13CO}$ phase. Small solid and open circles represent the CO molecules in nearly top and bridge sites, respectively. Large circles in different shades of gray represent the Pt atoms in three groups with-

different rotation centers. The “side view” is not a projection, but a simplified picture to illustrate schematically the grouping and layer expansion. The top layer expansions of 0.28 and 0.04 from the lattice positions are amplified 4-fold for simplicity (taken from Ref. [36]).

der the near-top sites and the near-bridge site CO molecules. The top view (Fig. 1.1) shows how the 19 Pt atoms in the top-layer of the “ $\sqrt{19}$ ” unit cell are grouped into a motif that contains 7 Pt atoms in a centered-hexagon region and 12 Pt atoms that are split between two triangular regions. Within each group, the Pt atoms are allowed to expand/contract laterally and to rotate around their center. For the underlying layers, the Pt atoms are assigned to either a centered-hexagon or a triangular region based on the ABC stacking sequence. This feature is illustrated schematically by the simplified “side view” shown in Fig. 1.1. These results demonstrate that, if adsorption is relatively strong, then subsurface atoms can move collectively to form a pattern on the nanometer scale that is determined by the unit cell of an adlayer. The ability to probe the relaxation in sub-surface layers at the metal/electrolyte interface is unique to the SXS technique, and this kind of surface restructuring cannot be studied by any other experimental methods.

The study of relaxation phenomena at monometallic/electrolyte interfaces has recently been extended to bimetallic surfaces. The $H_{\text{upd}}(\text{OH}_{\text{ad}})$ -induced³⁾ changes in the surface relaxation of a bulk $\text{Pt}_3\text{Sn}(111)$ bimetallic alloy have been studied by SXS and CV measurements [31]. From fits to CTR data, using a structural model in which the vertical displacement (Δd_{Pt} , Δd_{Sn}), surface coverage (θ_{Pt} , θ_{Sn}), and roughness (σ_{Pt} , σ_{Sn}) of the Pt and Sn in the topmost two atomic layers were allowed to vary, it was found that expansion of the surface Pt atoms induced by the adsorption of hydrogen was very similar to that observed on Pt(111) [35, 37] (at 0.05 V $\Delta d_{\text{Pt}}^1 = +2\%$). As shown in Fig. 1.2, XRV at (1, 0, 3.6) and (1, 0, 4.3) indicate that the desorption of hydrogen, as well as the adsorption of bisulfate anions, leads to surface contraction, i.e. the interplanar spacing, shown as Δd in the insert of Fig. 1.2b, decreases monotonically by scanning the potential positively from 0.05 V. At 0.55 V the Pt surface atoms are unrelaxed whereas the Sn atoms in the topmost layer expand up to $\Delta d_{\text{Sn}}^1 = 8.5\%$ of the lattice spacing, i.e. the surface becomes increasingly *buckled* as the Sn atoms expand outwards. The onset potential of Sn dissolution is determined by the potential at which the bulk termination of the $\text{Pt}_3\text{Sn}(111)$ lattice begins to disorder. It is interesting that, in the presence of CO⁴⁾, the potential range of surface stability is wider than in CO-free solution, an effect which strongly resembles the CO-controlled “rec” \leftrightarrow (1 \times 1) transition of Au(*hkl*) in alkaline solution (the latter is discussed in Section 1.3.2). It has been proposed that the reason for the increased potential range of stability of the $\text{Pt}_3\text{Sn}(111)$ surface in the presence of CO arises because of the continuous consumption of OH in the Langmuir-Hinshelwood (L-H) reaction ($\text{CO}_{\text{ad}} + \text{OH}_{\text{ad}} = \text{CO}_2 + \text{H}^+ + \text{e}^-$). In this reaction, OH is adsorbed on Sn surface atoms whereas CO is exclusively adsorbed on Pt atoms. Note that, in the H_{upd} region, the adsorption of CO on the $\text{Pt}_3\text{Sn}(111)$ surface does not lead to the large surface relaxation (4%) observed

3) The nature of the oxygenated species adsorbed onto Sn is unknown but, for the sake of discussion, this species will be collectively designated OH_{ad} .

4) Details about the vibrational properties of CO on platinum bimetallic surfaces including the $\text{Pt}_3\text{Sn}(111)$ system are presented by Korzeniowski in Chapter 7.

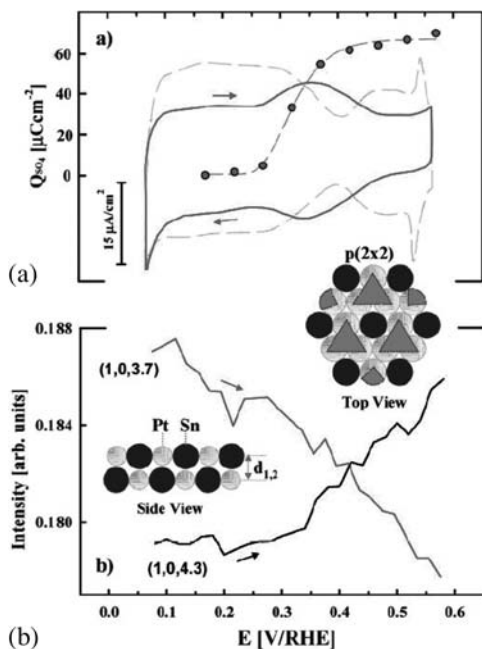


Fig. 1.2 (a) Cyclic voltammograms of Pt(111) (dashed line) and Pt₃Sn(111) (solid line) in 0.5 M H₂SO₄, scan rate 50 mV s⁻¹. Potential-dependent integrated charges for the adsorption of (bi)sulfate anions on the Pt₃Sn(111) surface are represented by circles. (b) The measured X-ray intensities at (1, 0, 3.7) and (1, 0, 4.3) as a function of

the electrode potential. Top and side views represent the proposed $p(2 \times 2)$ structure. The gray circles are Pt atoms, the black circles are Sn atoms, and triangles are (bi)sulfate anions which are adsorbed on Pt sites. The side view indicates the surface normal spacing that is derived from CTR measurements (taken from Ref. [30]).

on the Pt monometallic surface. This agrees with DFT calculations in which the binding energy of CO on Pt₃Sn(111) was calculated to be weaker than on Pt(111) [38]. As discussed below, however, on other bimetallic surfaces, in this case Pt/Pd, CO can produce large relaxation effects in the presence of H_{upd}.

The deposition of Pd onto Pt(*hkl*) and Au(*hkl*) surfaces has been studied by SXS, and a precise description of the Pd surface structure can be obtained by measuring and modeling the CTRs [32–34, 39]. This is particularly true for Pd/Pt(111) as, for coverages of up to 1 ML, Pd forms a pseudomorphic overlayer, i.e. it is fully commensurate with the Pt(111) lattice [28, 33]. The specular, (0, 0, *l*), and first-order, non-specular, (1, 0, *l*) and (0, 1, *l*), CTRs measured at 0.05 V for 1 ML of Pd on Pt(111) are shown in Fig. 1.3. The calculated CTRs for an ideally terminated Pt(111) surface are shown by the dashed curves, and this is close to the results obtained for the clean Pt(111) surface in electrolyte [37]. The data in Fig. 1.3 differ significantly from the model calculations at the “anti-Bragg” positions, midway between the Bragg reflections. At these positions, the scattering from the bulk Pt lattice is effectively canceled and the scattered inten-

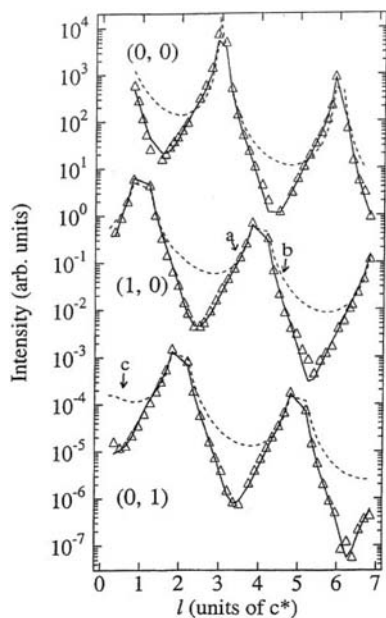


Fig. 1.3 The specular and first-order non-specular CTRs for the Pd/Pt(111) surface measured at an electrode potential of 0.05 V in CO-saturated solution. The dashed lines are calculated for an ideally terminated Pt(111) surface. The solid lines are a fit according to the structural model described in the text. The indicated positions (a, b, c) are those at which the data shown in Fig. 1.4 were measured (taken from Ref. [34]).

sity is due to the topmost Pt atomic layer and the Pd overlayer. Because of the difference in atomic form factor for Pt and Pd, this results in a significant decrease in intensity compared to the ideal Pt surface calculation [28]. The solid lines in Fig. 1.3 are a calculated best fit to the data using a structural model in which the Pd coverage (Θ_{Pd}), Pt-Pd distance ($d_{\text{Pt-Pd}}$), relaxation of the Pt surface (ϵ_{Pt}), and surface roughness parameters (σ_{Pd} , σ_{Pt}) were varied. The Pd atoms were located at Pt threefold hollow sites to continue the ABC stacking of the bulk lattice. The structural parameters obtained are $\Theta_{\text{Pd}} = 1.0 \pm 0.1$ monolayers (ML), $d_{\text{Pt-Pd}} = 2.32 \pm 0.02$ Å, expansion of the Pt lattice $\epsilon_{\text{Pt}} = 0.02 \pm 0.02$ Å and static Debye-Waller-type roughness, $\sigma_{\text{Pd}} = 0.12 \pm 0.04$ Å and $\sigma_{\text{Pt}} = 0.09 \pm 0.04$ Å. The Pt-Pd layer spacing corresponds to an expansion of $\sim 2.5\%$ relative to the Pt-Pt layer spacing, which is similar to the expansion observed on the monometallic Pt surface in the presence of H_{upd} .

The potential dependence of the surface relaxation and the stability of the Pd film was probed by XRV measurements [32]. Desorption of H_{upd} caused a slight Pt-Pd contraction, but the surface became expanded again ($\sim 2.5\%$) after the adsorption of bisulfate anions. At positive potentials, i.e. in the potential region of OH adsorption, there was a significant (but *reversible*) change in the Pd structure associated with oxide formation. Importantly, if the Pt(111) monometallic surface had been cycled up to this potential, then a Pt oxide would be formed that would lead to irreversible roughening (which is the precursor to Pt dissolution) of the surface upon reduction.

Adsorption of CO onto the Pt/Pd surface at 0.05 V also led to no significant changes in the Pt-Pd layer spacing (compared to a 4% expansion of the Pt mono-

metallic surface). This may indicate that the Pd-CO_{ad} interaction is weaker than the Pt-CO_{ad} interaction (an electronic effect) and/or is compensated by an even stronger Pt-Pd interaction, thus limiting the surface expansion. This conclusion is supported by the XRV measurements measured at three reciprocal lattice positions as the electrode potential was cycled over the range 0.05–1.15 V in CO-saturated solution (shown in Fig. 1.4). The (1, 0, 3.6) and (1, 0, 4.4) positions, on either side of the Pt (1, 0, 4) Bragg reflection, are principally sensitive to changes in the Pt-Pd spacing, provided that the Pd atoms remain commensurate with the Pt lattice. Thus, an increase in intensity at (1, 0, 3.6) and a corresponding decrease at (1, 0, 4.4) implies an expansion of the Pd-Pt surface and vice-versa. The (0, 1, 0.5) position is an “anti-Bragg” point, midway between the (0, 1, –1) and (0, 1, 2) Pt Bragg reflections and is primarily sensitive to the Pd coverage (as can be seen from the model calculations in Fig. 1.3). The data in Fig. 1.4 essentially show two structural effects which are separated in the figure by the vertical marker line at ~0.85 V. Considering only the anodic sweep, it is clear from the (0, 1, 0.5) data that no changes in the Pd surface coverage occurs over the range 0–0.85 V, the upper limit being the potential at which CO oxidation is occurring. The intensities at (1, 0, 3.6) and (1, 0, 4.4), however, show dramatic changes over this potential region consistent with a significant contraction in the Pd-Pt layer spacing. Such changes are not observed in CO-free solution [32]. As the intensities shown are normalized to the scattered intensity measured at 0.05 V, the change in the Pt-Pd spacing necessary to reproduce the intensity ratios, R ($R=0.8$ and $R=1.5$ for $l=3.6$ and $l=4.4$ respectively), can be calculated. For a Pd-Pt spacing of 2.25 Å, the calculated ratios are $R=0.80$ and $R=1.42$, which are in reasonable agreement with the experimental results. It is apparent, therefore, that the onset of the CO

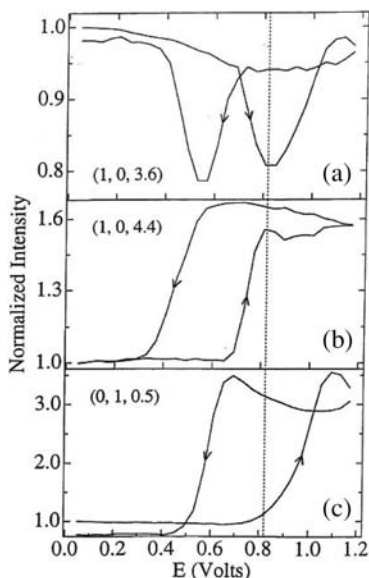


Fig. 1.4 The X-ray intensity measured at three reciprocal lattice positions (indicated in Fig. 1.3) as the potential was cycled over the range 0.05–1.15 V vs RHE (sweep rate = 2 mV s⁻¹). At each position the intensities are normalized to the intensity measured at 0.05 V. The vertical line marker denotes the two potential regions of interest (see text; taken from Ref. [34]).

oxidation reaction causes a large contraction ($\sim 1\%$ compared to the Pt-Pt bulk spacing) of the Pd-Pt surface. Given that the adsorbed CO molecules are reacting with OH species [presumably in an L-H reaction as observed for Pt(111)], it may be that the lattice contraction reflects the expected Pd-Pt bond length in the absence of strong chemisorption on the surface. In fact this bond length is in good agreement with a calculation of the Pt-Pd distance according to a hard sphere model using the atomic radii of Pt and Pd.

Pd films were also examined at successively higher levels of thickness, ranging from 1 ML to n ML ($n > 2$) regime. It was found that on the top of a pseudo-morphic monolayer film, Pd deposited on Pt(111) forms three-dimensional is-

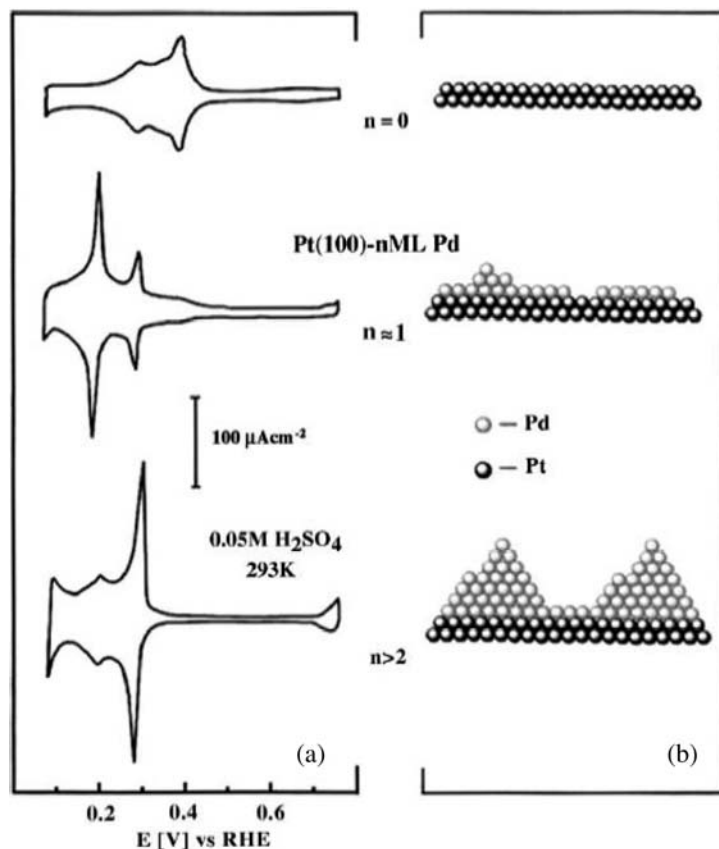


Fig. 1.5 (a) Cyclic voltammetry from the Pt(001) and Pt(001)-Pd surface in 0.05 M H₂SO₄ at a sweep rate of 20 mV s⁻¹. Subsequent to Pd deposition, sharp peaks arise at ~ 0.2 and 0.29 V which correspond to hydrogen adsorption/desorption accompanied by (b) sulfate desorption/

adsorption. The 0.29 V peak is due to adsorption/desorption at Pd step-terrace sites, which occur after the completion of the monolayer. (b) A schematic of the Pt(001)-Pd surfaces derived from CTR measurements at each level of Pd coverage (taken from Ref. [34]).

lands, implying that above 1 ML Pd deposition proceeds via a pseudomorphic Stranski-Krastanov growth mode [33]. The growth of Pd onto Pt(100) follows a similar mechanism to the Pt(111)-Pd system, with growth of the second Pd layer beginning after the first Pd layer reaches a coverage of 0.8 ML. As summarized in Fig. 1.5, further Pd deposition sees the formation of larger islands built onto the first Pd layer, characteristic of pseudomorphic S-K growth. For both Pt(111) and Pt(100) the SXS measurements provided the structural characterization that enabled interpretation of the voltammetric features (shown in Fig. 1.5). In the thick Pd films the lattice spacing in the Pd films was close to the bulk Pd lattice constant. Because of the complexity of the Pd film structure, XRV measurements showed no significant changes upon potential cycling, presumably as adsorption occurs at terrace and step sites on the defective Pd film and there is no concerted movement of surface atoms. Similarly, the effect of CO on the Pd_{nML}/Pt(100) structure in the H_{upd} region was negligible, i.e. measurements of the X-ray scattering signal at the surface expansion-sensitive CTR positions showed no change after saturation of the electrolyte with CO, although H_{upd} is displaced from the Pd surface by CO. In contrast, however, a dramatic change in the X-ray intensity was observed at -0.04 V (the hydrogen evolution region and the formation of H_{opd}). For full details, see [34]. Given that the same effect is not observed in CO-free electrolyte, it was proposed that the observed relaxation (determined as expansion of the bulk lattice constant of the Pd film by detailed CTR measurements) is caused by CO-induced hydrogen *absorption* into the Pd lattice. A promoting effect was explained through the change in local surface electronic structure, which gives rise to electron transfer between adsorbed CO and H_{upd} through the underlying metal, an explanation previously used to rationalize the promotion of hydrogen absorption on Pt modified by poisoning species such as P, S, As, Se, Sb [34, 40, 41]. Hydrogen absorption is important for energy storage systems, and this may be a research field in which SXS can make a significant contribution to the design of new materials.

1.3.1.2 Group IB Metals

In this section we briefly discuss the surface expansion of the group 1B metals, Cu, Ag and Au, focusing on the close-packed (111) surfaces as they have been studied in the most detail (in fact there have been no published SXS studies of the Cu(100) and Cu(110) surfaces in the electrochemical environment). In terms of surface expansion effects, the 1B metals are more difficult to study than Pt as no H_{upd} is formed, and so it is difficult to correlate structural changes with well-defined adsorption processes. Furthermore, the Au(*hkl*) surfaces reconstruct at negative potential, which limits the potential window where the surfaces are in the unreconstructed state. Despite these difficulties, relaxation at the Au(111) surface was recently studied by a combination of SXS and surface stress measurements. For potentials on the positive side of the potential of zero charge (pzc), where the surface is unreconstructed, increasing positive surface charge

causes a decrease in the tensile stress, a result that can be understood on the basis of a simple jellium model [42]. Correspondingly, one might expect that positive surface charge would lead to an increase in the surface expansion due to the apparent weakening of the surface bonds, but it was found that the opposite was true. Determination of the surface expansion of Au(111) in 0.5 M H_2SO_4 solution was obtained by XRV measurements at “expansion-sensitive” reciprocal lattice positions coupled with measurement and modeling of CTR data to calibrate the XRV results (in this case, the only parameter allowed to vary for data taken at different potentials was the expansion of the topmost Au atomic layer) [43]. The results show that close to the pzc the surface is expanded by $\sim 1.5\%$ of the bulk layer spacing and that this expansion decreases with increasing surface charge to $\sim 0.2\%$ at the positive potential limit. In order to rationalize the apparent conflict between the surface stress and surface expansion results, first principle density functional theory (DFT) calculations of Au(111) surface relaxation were made. For the uncharged surface the calculations gave an outward expansion of 1.3% of the bulk layer spacing, in remarkable agreement with the X-ray measurements. Based on these results, it was proposed that surface restructuring is a trade-off between cohesion between adjacent atoms and the band structure of the crystal. The density of states (DOS) for the relaxed surface is depleted near the Fermi level but enriched in the interval -4 eV to -1 eV below the Fermi level. The authors concluded that the shifting of the crystal bands to lower energies is the driving force for the outward expansion.

Surface restructuring at the Ag(111) electrode was examined as part of the study of the water structure at the metal/electrolyte interface by Toney and co-workers [44]. They measured the non-specular CTRs for the Ag(111) electrode in 0.1 M NaF to determine the Ag surface expansion independently of the incommensurate water layer and found that the surface was unrelaxed at a potential -0.23 V negative of the pzc and contracted by 0.03 Å (1.2% of the Ag(111) layer spacing ($d_{(111)} = 2.36$ Å) at a potential $+0.52$ V of the pzc). Although the importance of the electrostrictive effect was noted, it was not discussed in any detail; instead, the report focused on the interpretation of the specular CTR, which indicated the presence of a dense, “ice-like”, water layer at the interface. The presence of such a water structure at the interface has yet to be confirmed by any other experimental technique. Indeed, similar CTR measurements were obtained on a Cu(111) crystal in 0.1 M HClO_4 [45], and the data were interpreted in terms of an adsorbed monolayer of oxygen or OH (with no long-range order). It was postulated that such an adsorbed monolayer would explain the high density of the water layer proposed by Toney et al. [44].

Recently, Ag(111) in 0.1 M KOH was also studied by SXS [46], and, as in the previous study, the surface was characterized by measurement of the non-specular CTRs and specular CTR. In alkaline solution there is no competition between OH and anions for adsorption sites, and the SXS data can be interpreted purely on the basis of the surface coverage by OH_{ad} . At -0.95 V (vs SCE) the best fit parameters to the CTR data indicated that the surface layer undergoes a small *inward* relaxation (contraction) of $\sim 0.8\%$ of the Ag(111) layer spacing

($d_{(111)} = 2.36 \text{ \AA}$). At the positive potential limit (-0.11 V), where the coverage by OH is calculated to be $\sim 0.45 \text{ ML}$ from the CV, the surface contraction was increased to 1.2% of the Ag(111) layer spacing (identical to the measurement in 0.1 M NaF solution), and the modeling of the specular CTR indicated an OH coverage of $\sim 0.45 \text{ ML}$. Key insight into the potential dependence of the surface relaxation is given by the XRV measurements that are shown in Fig. 1.6, together with the cyclic voltammetry in Fig. 1.6a. The solid black (anodic) and dashed black (cathodic) lines in Fig. 1.6b represent the background subtracted intensity as a function of potential during cycling measured at the $(0, 0, 1.6)$ position on the specular CTR. The reversibility of the scattered intensity indicates that between these potential limits the adsorption of oxygenated species is a fully reversible process. Also shown is the OH coverage calculated from the charge under the CV (dash-dot line), showing a gradual increase in θ_{OH} , implying that change in the specular CTR is associated with OH adsorption. The behavior of the non-specular CTRs (used to measure the surface relaxation), however, reveals a new structural effect at -0.75 V (indicated in the figure by a vertical dashed line), a potential that is very close to the pzc [47]. Fig. 1.6c shows the X-ray intensity at $(0, 1, 0.5)$, a position on the $(0, 1, l)$ CTR sensitive to the surface termination of the Ag(111) crystal. In the positive-going sweep there is a significant dip in the intensity beginning at 0.9 V , going to a minimum at ca. -0.75 V , and followed by a partial recovery by -0.55 V . Following this there is a small continuous decrease in intensity over the range -0.55 V to 0 V . The onset of the decrease in intensity at -0.9 V is coincident with the start of OH^- adsorption on the surface, indicating that significant changes to the Ag surface structure are occurring with a relatively small OH coverage of less than 0.05 ML . Note also that this potential is very close to the pzc. The negative-going sweep shows the XRV to be fully reversible over the entire potential range.

It is important to note that the changes in intensity at the $(0, 1, 0.5)$ CTR position cannot be rationalized in terms of surface relaxation as this has a negligible effect on the intensity at an anti-Bragg position. The dip in intensity, therefore, must be attributed to a surface roughening type effect. *In-situ* UHV-STM measurements of low surface coverage ($\theta_{\text{O}} < 0.05 \text{ ML}$) of OH on Ag(111) indicated that oxygen randomly adsorbs with a large near-neighbor exclusion zone of approx. 12 Ag atoms for each O atom [48], whereas at coverage greater than $\sim 0.05 \text{ ML}$ a $p(4 \times 4)\text{-O}$ phase is observed [49]. In the electrochemical environment, STM results indicate that, for the Ag(111) surface, strong adsorption of OH causes 2D (in-plane) stretching of the surface layer [50], and this may account for the changes observed in Fig. 1.6c.

For the group 1B metals there appears to be a correlation between the pzc (surface charge) and surface relaxation. In contrast to $\text{Pt}(hkl)$ surfaces, the $\text{Ag}(hkl)$ surfaces ($\text{Ag}(100)$ and $\text{Ag}(110)$ also exhibit inward relaxation [46]) undergo surface contraction that increases as the coverage by OH_{ad} increases. In the case of $\text{Au}(hkl)$, the trend toward surface relaxation is difficult to extract because of the reconstruction of the surfaces at negative potential. In the unreconstructed state, however, it appears that the surfaces also contract as the coverage

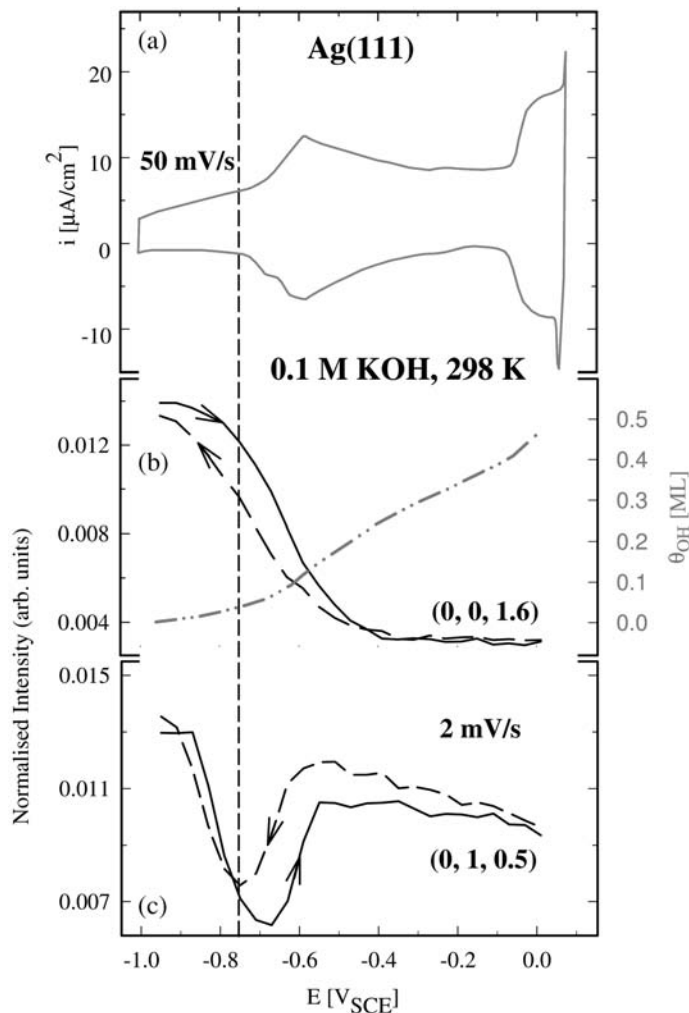


Fig. 1.6 (a) Cyclic voltammetry of Ag(111) in 0.1 M KOH recorded at a sweep rate of 50 mV s^{-1} , (b) X-ray voltammetry (XRV) measured at an “anti-Bragg” position on the specular CTR (solid and dashed lines), a position sensitive to the effects of adsorbates on the surface; the potential-

dependent coverage by OH_{ad} , assessed from the CV, is shown as a dash-dot line, (c) XRV measured at (0, 1, 0.5) showing reversible structural changes triggered by adsorption of OH at low surface coverages ($\sim 0.05 \text{ ML}$) (to be published).

by oxygenated species increases. At present we do not have a definitive explanation for these effects; however, the differences in electronic structure between Pt group metals and the 1B group metals may be the key to understanding the relaxation behavior.

1.3.2

Surface Reconstruction

It is now well established that in UHV the clean low-index faces of some *fcc* metals tend to exhibit reconstruction under certain conditions of sample temperature and surface preparation. This is certainly true of Pt and Au, whereas most other *fcc* metals, such as Cu, Ni, and Ag, do not reconstruct. The tendency of the clean Pt and Au surfaces to reconstruct in UHV has been explained by Ho and Bohnen using first-principles calculations [51] and later by Norskov using a combination of local density functional calculations and modeling within the effective medium theory [52]. Both studies predicted that the participation of *d* electrons in bonding in the solid and the decrease of the kinetic energy of delocalized electrons at the surface play a decisive role in the stabilization of the experimentally observed missing-row reconstructions of Au(110) and Pt(110) surfaces. Several experiments also illustrated that, in the UHV environment, the adsorption of atoms and molecules on clean metal surfaces has a dramatic effect on the metal surface relaxation and can cause clean metal surfaces to reconstruct or to deconstruct (“lift”) back to the (1×1) phase [28]. The thermodynamic driving force for adsorbate-induced restructuring is the formation of strong adsorbate-substrate bonds that are comparable to, or stronger than, the bonds between the substrate atoms in the clean surface. Although the same thermodynamic effects may be valid in electrochemistry, significant differences in adsorbate-induced restructuring in UHV and in electrochemical systems have been observed. As has been demonstrated [28, 29], these differences can be accounted for in terms of (a) the presence of co-adsorbed solvent and adsorbed species, and (b) differing surface potentials (φ) and (continuously adjustable) variations in electrode potential. The former effect results in the formation of an adsorbed layer of water, the adsorption of hydrogen, reversible/irreversible formation of oxygenated species, and the adsorption of anions from supporting electrolyte. The latter effect results in potential-induced changes of the surface electron density. As demonstrated below, although in an electrochemical environment thermodynamic and/or electronic effects are difficult to decouple, taken together these two effects play a major role in determining surface restructuring in electrochemical systems.

Given that adsorbate-induced lifting of reconstruction is observed only at Au(*hkl*)/solution interfaces, we focus on the transition between the reconstructed (“rec”) and (1×1) phases of Au(*hkl*) surfaces in the electrochemical environment. Simplified real space models for the bulk-terminated and reconstructed low-index surfaces of gold are depicted in Fig. 1.7. The reconstructions of the Au(*hkl*) surfaces are observed at negative potentials where the surfaces are (almost) free of strongly adsorbing anions. For Au(111), the reconstruction is rather complex and involves a small increase in the surface density, which leads to a large unit cell, with a $(23 \times \sqrt{3})$ periodicity [53, 54]. The Au(110) surface exhibits either (1×2) or (1×3) periodicity [54, 55]. The (1×2) phase is called the “missing row” structure, since every other row is lost in going from the

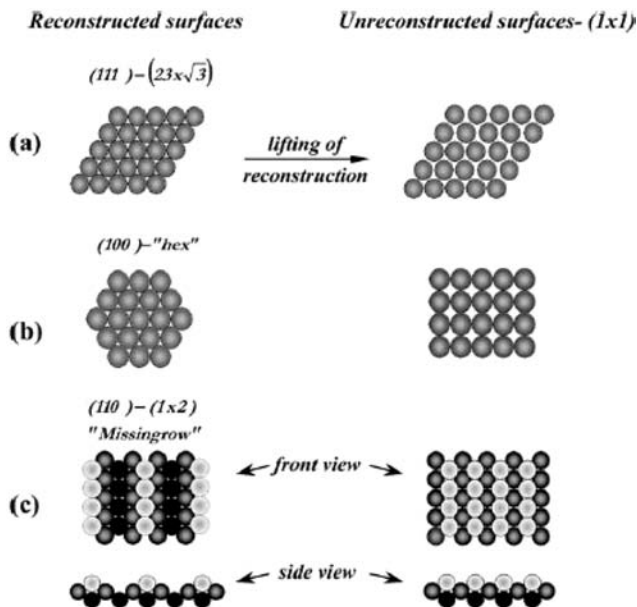


Fig. 1.7 Simplified real space model of reconstructed (left side) and bulk terminated (right side) $\text{Au}(hkl)$ surfaces: (a) $\text{Au}(111) - (23 \times 3) \leftrightarrow (1 \times 1)$; (b) $\text{Au}(111) - (5 \times 20) \leftrightarrow (1 \times 1)$; (c) $\text{Au}(110) - (1 \times 2) \leftrightarrow (1 \times 1)$ (taken from Ref. [59]).

(1×1) phase to the (1×2) phase, and, as a result, the surface atomic density changes very significantly, by 50%! The $\text{Au}(100)$ surface exhibits a hexagonal reconstruction which consists of a single, buckled, slightly distorted overlayer, which is aligned close to the $[110]$ bulk direction and is often referred to as a "5x20" or "hex" reconstruction [2, 9]. The results presented in this section are for the $\text{Au}(100)$ surface, and Fig. 1.8 shows representative in-plane X-ray diffraction results in the form of rocking scans through reciprocal lattice positions where scattering from the reconstruction is observed. In 0.1 M HClO_4 the scan always displays two peaks, which are rotated by $\sim 0.75^\circ$ from the $[110]$ direction. In 0.1 M KOH , however, the scan shows either a single broad peak aligned with the $\text{Au}[110]$ direction [9] or two peaks rotated by 0.75° from the $[110]$ direction. Based on the fact that the peaks are much broader, it was suggested that the structure in alkaline solution is more pinned to defects which may hinder the rotation [56].

The lifting of the reconstruction is found to be potential-dependent, and each surface has its own dynamics in the "rec" $\leftrightarrow (1 \times 1)$ conversion, which is associated with significant surface mass change. Of particular interest in this regard has been the behavior of $\text{Au}(100)$ in alkaline as well as in acidic electrolytes, and this section therefore focuses on the adsorbate-induced "hex" $\leftrightarrow (1 \times 1)$ transition on this surface. Although only results for the adsorbate-induced recon-

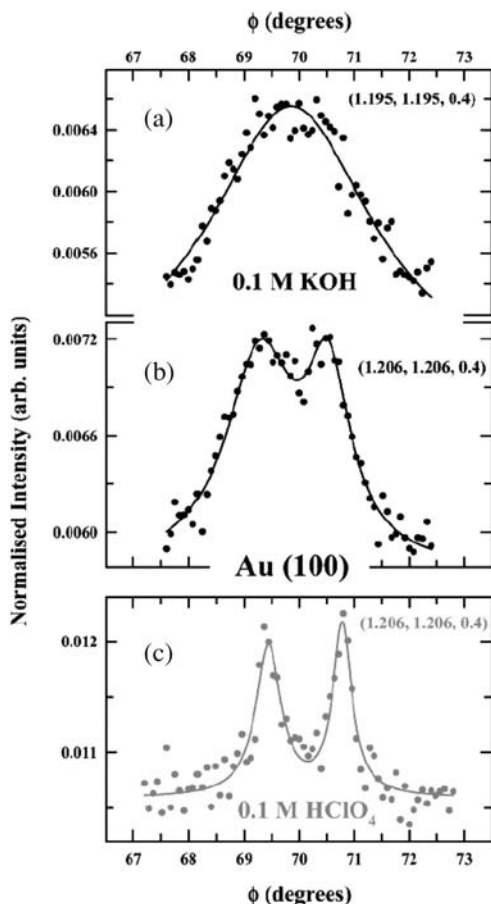


Fig. 1.8 Rocking scans through: (a) (1.195, 1.195, 0.4) and (b) (1.206, 1.206, 0.4) in 0.1 M KOH and (c) (1.206, 1.206, 0.4) in 0.1 M HClO₄ at 0.05 V vs RHE. At these reciprocal space positions, scattering from the reconstructed “hex” phase is observed (taken from Ref. [56]).

struction of the Au(100) surface are shown, the conclusions are rather general and equally applicable to the Au(111) and Au(110) systems (see [29]).

The potential range of stability as well as the dynamics of formation/lifting of the “hex” phase in alkaline solution have been analyzed by a combination of SXS and cyclic voltammetry [56]. A significant feature of the voltammetry in 0.1 M KOH, depicted in Fig. 1.9a, is the pseudocapacitance peak appearing at ~ 1.0 V. The sharp peak at 1.0 V was initially suggested to be associated with the potential/(OH_{ad})-induced lifting of the “hex” reconstruction, by analogy with the related peaks observed in acid solution containing strongly adsorbing anions [7]. It is interesting that XRV measurements at the reconstruction-sensitive reci-

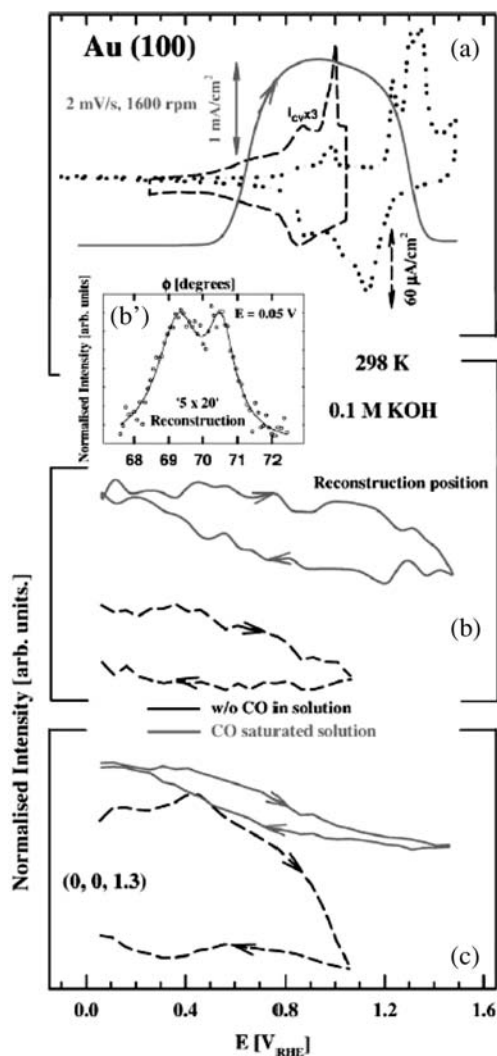


Fig. 1.9 (a) The cyclic voltammetry for Au(100) in 0.1 M KOH along with the polarization curve for CO oxidation in CO-saturated solution (continuous curve); (b) XRV measured at the reconstruction position (1.206, 1.206, 0.4) in CO-free (dashed curve) and CO-saturated (solid line)

solution; (b') rocking scan through (1.206, 1.206, 0.4); (c) XRV measured at a position sensitive to the mass transfer involved in the surface reconstruction, (0, 0, 1.3), with and without CO in solution (taken from Ref. [59]).

procal space position in Fig. 1.9b unambiguously show that the onset of lifting of the “hex” phase takes place below 1.0 V. (Fig. 1.9b shows in-plane X-ray diffraction results in the form of rocking scans through reciprocal lattice positions where scattering from the reconstruction is observed.) As a result, the kinetics

of “hex” formation is rather slow, as demonstrated in Fig. 1.9c at the specular CTR position sensitive to the mass transfer involved in the surface reconstruction. In fact the lifting of the reconstruction follows the adsorption isotherm of OH_{ad} . This implies that the lifting of the reconstruction is adsorption-induced rather than an electric field effect.

Further insight into the “electric field vs adsorption” issue has been obtained by monitoring the surface reconstruction under conditions in which strongly adsorbed OH_{ad} is removed from the surface by a relatively weakly adsorbed reactant, namely CO_{ad} . (For details of the vibrational properties of CO on Pt and Au see Korzeniewski’s Chapter 7.) Surprisingly, it has been found that CO acts to catalyze the formation of uniform reconstructed domains. This phenomenon was established initially by STM studies of the Au(100) surface in alkaline solution [58] and was reexamined using SXS. The key results are shown in Fig. 1.9, which, in addition to the CV/XRV measurement in nitrogen-purged 0.1 M KOH solution, also summarizes the results in CO-saturated 0.1 M KOH. The new information provided by the SXS results was that the slow kinetics of the formation of the reconstruction observed in N_2 -purged alkaline solution is much faster in CO-saturated solution (Fig. 1.9c), and, even more remarkably, the reconstruction is present over the entire potential range, i.e. up to 1.5 V in Fig. 1.9b. Gallagher et al. [59] showed that the CO-induced changes in the “rec” \leftrightarrow (1 \times 1) phase transition are not unique to the Au(100) surface but rather constitute a general phenomenon, which, on all three Au single-crystal surfaces, is induced by continuous removal of strongly adsorbed OH by weakly adsorbed CO in the L-H reaction. The fact that the potential range of stability of the reconstructed surfaces is so extended in the presence of CO (up to 1.7 V!) indicates that lifting of the reconstruction is determined by energy of adsorption rather than by the electric field.

Further evidence for this conclusion was obtained in acid solution, where anions and OH_{ad} are in strong competition for the adsorption sites. To minimize the effects of OH_{ad} and to emphasise the effect of anions, results were obtained for Au(100) in 0.1 M HClO_4 before and after Br^- anions were added to solution. An overview of the electrochemical and SXS results is given in Fig. 1.10. As has been discussed recently [60], similarly to the effect of Cl_{ad} on the thermodynamics/dynamics of the “hex” \leftrightarrow (1 \times 1) transition, the specific adsorption of Br^- shifts the equilibrium potential of the “hex” \rightarrow (1 \times 1) transition to less positive values (from Fig. 1.10b ca. 0.3 V) relative to Br^- -free solution. From analysis of SXS data, Blizanac et al. concluded that, although the specific adsorption of Br acts to catalyze the mobility of gold surface atoms, the formation of uniform “hex” domains is not enhanced by this movement [60]. Further inspection of Fig. 10a and b reveals that the “hex” \rightarrow (1 \times 1) transition is completed at ca. 0.1 V, or, based on the X-ray intensity measured at (0.5, 1, 0.15) in Fig. 1.10c, just before the formation of the $c(\sqrt{2}\times\sqrt{2})\text{R}45^\circ$ Br_{ad} superstructure (the latter will be discussed in Section 1.4.1). SXS results obtained in solution containing CO are also plotted in Fig. 1.10. Interestingly, in contrast to alkaline media (pH=13), Fig. 1.10b shows that CO has a negligible effect on the potential-de-

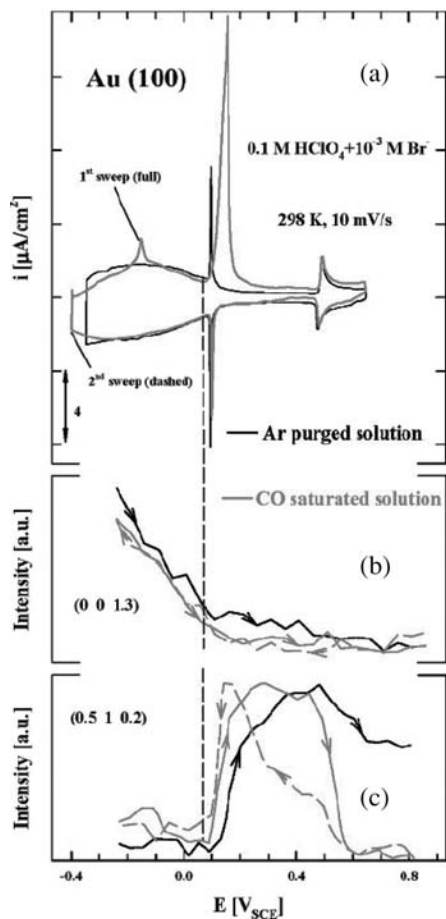


Fig. 1.10 (a) Current-potential curves (first scan) for Au(100) in 0.1 M $\text{HClO}_4 + 10^{-3}$ M Br^- purged with either argon (black curve) or CO (grey curve) at 10 mV s^{-1} ; (b) Corresponding XRV measurements

(2 mV s^{-1}) at (0, 0, 1.3), a position on the specular CTR; (c) XRV measurements (2 mV^{-1} s) at (0.5, 1, 0.2), where scattering from the $c(\sqrt{2} \times \sqrt{2})\text{R}45^\circ$ structure of Br_{ad} is observed (taken from Ref. [60]).

pendent XRV measured at the (0, 0, 1.3) position. Thus, at $\text{pH}=1$ in the presence of CO, the “hex” \leftrightarrow (1 \times 1) transition is shifted *negatively* by ca. 40 mV. This apparently opposite effect from that observed in Fig. 1.9 for alkaline solution has been explained on the basis of a CO-induced increase in the equilibrium Br_{ad} surface coverage relative to that at the same potential in CO-free solution. Given that the same effect is also observed for the other two low-index Au single crystals it is important to rationalize the opposite behavior observed for the “rec” \leftrightarrow (1 \times 1) transition in acid versus alkaline electrolyte. Blizanac et al. proposed that the pH-dependent CO effect is controlled by a delicate balance between the nature of the interaction of adsorbates with the Au(hkl) surface (the

energetic part) and the potential-dependent surface coverage by anionic species [60]. In particular, the energetic part is determined by the strength of the Au(*hkl*)-adsorbate interaction, the Au(*hkl*)-CO interaction being much weaker than the Au(*hkl*)-OH_{ad} interaction and, in particular, than the Au(*hkl*)-Br_{ad} interaction. As a result, OH_{ad} and Br_{ad} cannot be displaced from the Au(*hkl*) surface by CO, but, in contrast to Br_{ad}, OH_{ad} can be oxidatively removed from the surface in the L-H reaction. On this basis it was suggested that the equilibrium surface coverage by Br_{ad} and thus the “equilibrium” potential for the “rec” \leftrightarrow (1 \times 1) transition is a consequence of the CO-correction to the adsorption isotherm of Br_{ad}. As shown in Fig. 1.10c and discussed in Section 1.4, the fact that CO and OH_{ad} can react on the Au(100)-Br_{ad} surface determines the potential stability of the formation of the Br_{ad} c($\sqrt{2}\times\sqrt{2}$)R45° structure.

1.4

Adlayer Structures

The chemisorption of atoms or molecules onto monocrystalline metal surfaces characteristically yields ordered adlayer structures. This ordering can be understood, in general terms, from a balance between the preference for adsorbate bonding in specific coordination sites and the dominant adsorbate-adsorbate interaction at higher coverages. This leads to a rich variety of structural behavior that is ideally suited to study by SXS because of the high resolution of the technique, and a comprehensive list of these studies is given in the References. In this section, a brief review of these experiments is given. The first part describes the adsorption of anions, which is, in addition to the substrate-anion interaction, controlled by the competitive adsorption between anions and OH_{ad}. The second part describes the adsorption of CO onto Pt(111) and the effects of solution temperature on the CO structure and kinetics. Section 1.4.3 describes the driving force for the ordering of metal adlayers, such as reversible formation of metal UPD adlayers including co-adsorption of UPD cations and anions. The elucidation of this structural behavior, from a standpoint of both ordering of adlayers on *fcc* metal electrodes as well as electrochemical reactivity, is as significant in model systems as it is in systems of practical importance. Some important limitations in terms of understanding electrocatalytic activity should, however, be pointed out:

- In many systems it is difficult to find a correlation between the adsorbate structures that are formed and the catalytic behavior, as well-defined adsorbate structures of spectator species tend to block active surface sites.
- Most reaction intermediates, particularly those of importance to fuel cell reactions, tend not to form ordered structures and cannot be studied by SXS.

1.4.1

Anion Structures

The adsorption of anions on metal electrodes has been one of the major topics in surface electrochemistry. Specific adsorption of anions occurs when the anion loses all or part of its solvation shell and forms a direct chemical bond with the substrate. In this situation the surface coverage by anions can be high and the adlayer tends to form a close-packed structure that depends critically on the surface atomic geometry of the underlying substrate and the balance between the anion-metal and anion-anion interaction energies. The structures of halide anions adsorbed onto Au(*hkl*), Ag(*hkl*), and Pt(*hkl*) low-index surfaces have been the most widely studied systems by SXS, and a comprehensive review of ordered anion adlayers on metal electrodes is given by Magnussen [57].

On the close-packed (111) surfaces, halide anions form hexagonal overlayers that undergo electrocompression, and a variety of structures are observed: commensurate, incommensurate, uniaxially incommensurate, and rotated phases. On the more open (100) and (110) metal surfaces the symmetry of the substrate differs from the energetically-favorable hexagonal symmetry of the halide adlayers, and, in addition, the corrugation potential is higher, and this favors the formation of low-order commensurate phases. In fact, on (100) surfaces the most commonly observed structure is the $c(2\times 2)$ phase, a structure with a simple square symmetry and a surface coverage of 0.5 adatoms per metal surface atom. This structure has been observed on Ag(100), Cu(100), Pt(100), and Pd(100) for Cl^- , Br^- and I^- halide anions despite the fact that the atomic size mismatch can lead to large anion-anion bond lengths compared to the bond lengths found in the corresponding hexagonal phases [61–64].

It is only on the Au(100) surface that the anion-anion interaction is sufficient to perturb the influence of the substrate corrugation potential. For example, the bromide adlayer on Au(100) undergoes a commensurate-incommensurate transition where a commensurate $c(\sqrt{2}\times 2\sqrt{2})R45^\circ$ structure transforms continuously to an incommensurate $c(\sqrt{2}\times p)R45^\circ$ structure [65]. The CV for Au(001) in 0.05 M NaBr is shown in Fig. 1.11. Three sharp peaks (labeled by P1, P2, P3) are observed as the potential is swept between -0.25 V and 0.6 V; P1 corresponds to the lifting of the Au reconstruction to leave the surface in the (1×1) state, P2 corresponds to the formation of the $c(\sqrt{2}\times 2\sqrt{2})R45^\circ$ structure (as shown in Fig. 1.11 by the intensity changes at the $(0, 1, 0.1)$ reciprocal space position, which is where scattering from such a structure would arise), and P3 corresponds to the commensurate-incommensurate phase transition. The $c(\sqrt{2}\times 2\sqrt{2})R45^\circ$ structure is shown schematically in Fig. 1.12a, which indicates that the surface coverage by bromide is $\Theta=1/2$ and that the structure is close to a hexagonal arrangement, despite the square symmetry of the underlying substrate. This implies that the elastic interactions between the relatively large Br adatoms (which would favor hexagonal packing) dominate over the adsorbate-substrate interaction. The observed in-plane diffraction pattern is shown in Fig. 1.12c, where the squares correspond to substrate reflections and the circles

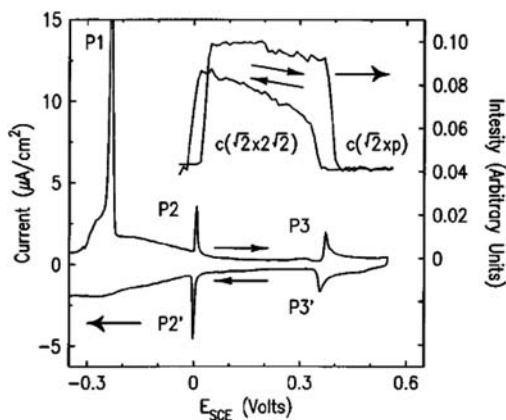


Fig. 1.11 The CV for an Au(100) electrode in 0.05 M NaBr solution and the corresponding X-ray intensity at the position (0, 1, 0.1) where scattering from a bromide adlayer was observed (taken from Ref. [65]).

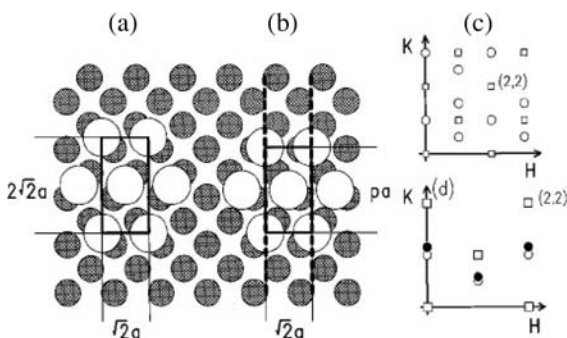


Fig. 1.12 Real space model (a, b) of the commensurate $c(\sqrt{2} \times 2\sqrt{2})R45^\circ$ and incommensurate $c(\sqrt{2} \times p)R45^\circ$ bromide structures observed on Au(001). The open circles correspond to bromide atoms and closed circles correspond to gold atoms;

(c) and (d) show the corresponding in-plane reciprocal space patterns where the squares are scattering from the Au substrate and the circles are Br reflections. In (d) the peaks move outward along K with increasing potential (taken from Ref. [65]).

to Br reflections. At potentials positive of P3 (0.38 V vs SCE), the bromide adlayer undergoes a commensurate-incommensurate transition, which was signified by the movement of the low-order diffraction features continuously and uniaxially outward with increasing potential. As shown in the diffraction pattern (Fig. 1.12 d), reflections were only observed at $(1, 0.5 + \varepsilon/2)$, $(0, 1 + \varepsilon)$ and $(2, 1 + \varepsilon)$, along with symmetry equivalents (ε denotes the incommensurability). The real-space model of the structure is shown in Fig. 1.12 b. For the domain shown, the bromide lattice is commensurate along H (the $\sqrt{2}$ direction) and incommensurate along K. As the potential increases above 0.38 V, the value of ε

increases continuously, and this corresponds to movement of the bromide atoms along the directions shown by the dashed lines in Fig. 1.12b. In the incommensurate phase the Br nearest-neighbor spacing is fixed at 4.078 Å, whereas the next-nearest-neighbor spacing decreases from 4.56 Å ($\varepsilon=0$, commensurate) to 4.14 Å ($\varepsilon=0.13$). This latter spacing is close to the minimum value observed on the Au(111) surface (4.02 Å).

Very recently, in an attempt to understand the competitive adsorption between Br_{ad} and OH_{ad} species and probe the role of OH_{ad} on the formation of the ordered bromide adlayer on Au, the Au(100)- Br_{ad} system was reexamined in both acidic and basic media. In line with the discussion in Section 1.3.2, the role of OH_{ad} was established by monitoring the microscopic interface structures of Br_{ad} during the consumption of OH_{ad} in an electrochemical reaction in which strongly adsorbed OH_{ad} is removed from the surface by relatively weakly adsorbed CO_{ad} . This follows the same methodology used to probe the effect of Cl_{ad} and Br_{ad} on the Au(100) surface reconstruction, as described in Section 1.3.2. We may recall that, because of oxidative removal of a small amount of OH_{ad} in the L-H reaction and an equivalent increase in the equilibrium Br_{ad} surface coverage, in the presence of CO the “hex” \leftrightarrow (1 \times 1) transition is shifted negatively by ca. 40 mV (Fig. 1.10c). Although the increase in $\Theta_{\text{Br}_{\text{ad}}}$ and the shift of the “hex” \leftrightarrow (1 \times 1) transition in solution saturated with CO is rather small, adsorption of CO has a significant effect on the ordering of the $c(\sqrt{2}\times\sqrt{2})\text{R}45^\circ$ structure, as shown in Fig. 1.10c. Analysis of rocking curves through the (0.5, 1, 0.2) reflection measured at 0.4 V, with and without CO in solution (Fig. 1.13), revealed that the domain size of the structure increases from 200 Å in CO-free solution to 230 Å in solution saturated with CO. As shown in Fig. 1.10c, in the presence of CO the onset of formation of the commensurate $c(\sqrt{2}\times\sqrt{2})\text{R}45^\circ$ structure is shifted negatively by ca. 40 mV, equal to the value of the thermodynamic potential shift of the “hex” \leftrightarrow (1 \times 1) transition in Fig. 1.10b. This reflects the fact that the complete transition of the “hex” phase into the (1 \times 1) phase is required in order to form the $c(\sqrt{2}\times\sqrt{2})\text{R}45^\circ$ structure. Further inspection of Fig. 1.10c reveals that, in the presence of CO, the $c(\sqrt{2}\times\sqrt{2})\text{R}45^\circ$ structure develops/disappears more rapidly than in solution free of CO, i.e., comparison of the XRV data shows that both the disorder-order transition and the commensurate-incommensurate transition are much sharper in the presence of CO. The observed CO effects on the formation of the $c(\sqrt{2}\times\sqrt{2})\text{R}45^\circ$ structure can be rationalized with the same argument as for the reconstruction phase transition in Fig. 1.9c, i.e., at the same electrode potential the Br_{ad} coverage may increase in CO-saturated solution because the competing OH_{ad} species are removed from the surface in the L-H reaction. As a consequence, the surface coverage by Br_{ad} required to form the $c(\sqrt{2}\times\sqrt{2})\text{R}45^\circ$ order adlayer ($\Theta_{\text{Br}_{\text{ad}}}=0.5 \text{ ML}$) may be established at lower potentials in the presence of CO. Such a mechanism would correlate nicely with the weak adsorption of CO on Au surfaces [23, 66], i.e., the Au(100)- Br_{ad} and Au(100)- OH_{ad} interaction is much stronger than the Au(100)-CO interaction and only Br_{ad} and OH_{ad} are competing for the surface sites.

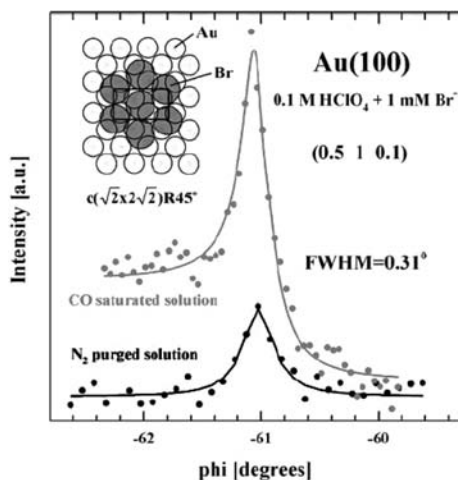


Fig. 1.13 Rocking scans through the (0.5, 1, 0.15) reciprocal lattice position measured at 0.4 V in the absence of CO (upper curve) and in the presence of CO (lower curve), where scattering from the commensurate $c(\sqrt{2} \times 2\sqrt{2})R45^\circ$ structure of the Br_{ad} adlayer in 0.1 M $\text{HClO}_4 + 10^{-3}$ M Br^- is

observed. The solid lines are fits of a Lorentzian line shape to the data which gives a coherent domain size for the $c(\sqrt{2} \times 2\sqrt{2})R45^\circ$ structure of ~ 150 Å. Also shown is a schematic picture of the $c(\sqrt{2} \times 2\sqrt{2})R45^\circ$ unit cell (taken from Ref. [60]).

The proposed effect of CO on competitive adsorption between Br^- and OH^- was further examined in alkaline solution. In particular, one may expect that the removal of OH_{ad} from the Au(100) surface by weakly adsorbed CO may allow the Br_{ad} adlayer to order, as it does in acid solution. To probe the CO effect on the ordering of the Br_{ad} adlayer, an “ h ” scan through the (1/2, 1, 0.15) peak due to the $c(\sqrt{2} \times 2\sqrt{2})R45^\circ$ structure was measured at 0.2 V, before and after saturating the solution with CO (Fig. 1.14). From Fig. 1.14, whereas in the absence of CO no ordered structure with the $c(\sqrt{2} \times p)R45^\circ$ symmetry is observed, in the presence of CO a sharp peak is found at the commensurate position ($h=0.5$). The insert of Fig. 1.14 shows a rocking scan at a Bragg reflection due to the $c(\sqrt{2} \times 2\sqrt{2})R45^\circ$ adlayer of Br_{ad} that is formed in the presence of CO. From the Lorentzian line shape fit (solid line) to this data, a domain size of ca. 200 Å is calculated, which is close to the domain size measured in acid solution. The potential dependence of the X-ray intensity at the (1/2, 1, 0.15) position (not shown, see Fig. 7 in [67]) revealed that a commensurate $c(\sqrt{2} \times 2\sqrt{2})R45^\circ$ structure is stable within ca. 0.3 V. At rather positive potentials, however, the commensurate-incommensurate transition is observed to be as reversible as in acid solution. In CO-free solution, neither a commensurate nor an incommensurate structure is found, presumably because of the strong competition between Br_{ad} and OH_{ad} in alkaline solution. Based on these observations, it has been proposed that the competitive adsorption between halide anions and oxygenated species may also play a significant role in the continuous transition

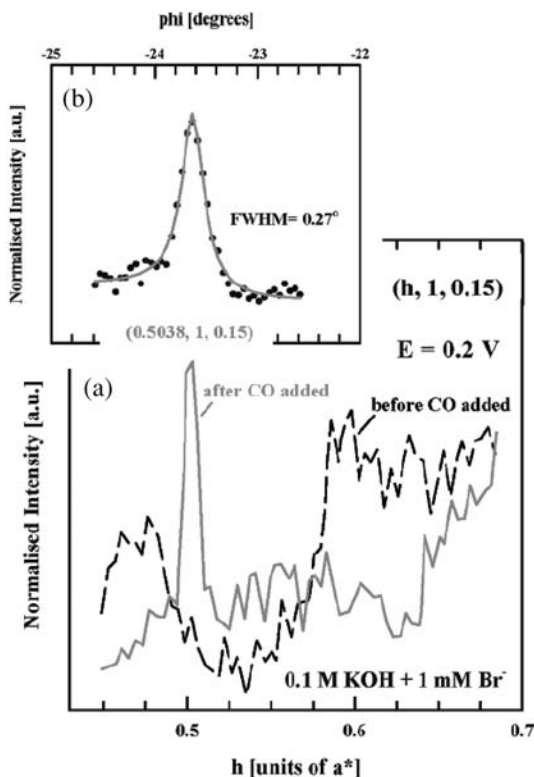


Fig. 1.14 (a) h -scans at $E=0.2 \text{ V}$ through the $(1/2, 1, 0.15)$ position before (dotted curve) and after (continuous curve) saturating $0.1 \text{ KOH} + 10^{-3} \text{ M Br}^-$ solution with CO. (b) Rocking scans through the $(1/2, 1, 0.15)$ reciprocal lattice position, where scattering from the commensurate $c(\sqrt{2} \times 2\sqrt{2})R45^\circ$

structure of the Br_{ad} adlayer is observed. The peak is only observed in CO-saturated solution. The solid lines are fits of a Lorentzian line shape to the data, which gives a coherent domain size for the $c(\sqrt{2} \times 2\sqrt{2})R45^\circ$ structure of ca. 175 \AA (taken from Ref. [60]).

from the commensurate $c(\sqrt{2} \times 2\sqrt{2})R45^\circ$ structure to the incommensurate $c(\sqrt{2} \times p)R45^\circ$ structure [68]. While a detailed understanding of the role of OH_{ad} on the phase transition in the Br_{ad} adlayer is not yet possible, the present discussion suggests that Br_{ad} compressibility may be determined not only by the adsorbate-adsorbate interaction [65, 68] but, in addition, by strong competition for Au adsorption sites between Br_{ad} and OH_{ad} . Competitive adsorption between anions and OH also plays a key role in the potential stability and ordering of many adsorbates, the prominent example being the interaction between CO and UPD metal adlayer structures on $\text{Pt}(hkl)$. This is described in more detail in Section 1.4.3.

1.4.2

CO Ordering on the Pt(111) Surface

The surface electrochemistry of CO adsorbed on transition metal surfaces has been the subject of intense theoretical and experimental work (for an overview, see [28, 69, 70]). In these studies there has been an emphasis on linking the microscopic structure of the CO adlayer to the thermodynamics and other macroscopic electrochemical responses at electrified interfaces. Whereas information regarding macroscopic properties has come from classical electrochemical techniques [71–73], the chemical, physical, and structural properties on the atomic scale have been obtained from either a combination of *in-situ* STM and vibrational spectroscopy [74, 75] or SXS and vibrational spectroscopy [76]. The adsorptive and catalytic properties of CO adsorbed on platinum single crystals have been most widely studied. This is because the system offers an opportunity to gain basic understanding, which could ultimately lead to the design of new catalysts and also to an understanding of the activity pattern of Pt metal nanoparticles employed in fuel cells in the size range of a few nanometers. The upper part of Fig. 1.15 displays polarization curves for the oxidation of dissolved CO on Pt(111) in acid solution. According to Fig. 1.15, two potential regions can be distinguished, i.e., the so-called pre-ignition potential region is followed by the ignition potential region. The term “ignition potential” is analogous to the term “ignition temperature” in gas-phase oxidation. It is the potential at which the rate becomes entirely mass transfer limited. Although the rate of CO oxidation changes with electrode potential, it has been suggested that in both the pre-ignition potential region and at or above the ignition potential, the mechanism for CO oxidation obeys an L-H type reaction in which CO_{ad} reacts with $\text{OH}=\text{ad}$ [77]. It was also proposed that the active sites for OH adsorption are defects in the Pt(111) surface [77]. This was supported by the fact that the activity in the pre-oxidation region is strongly dependent on the pre-history of the electrode, i.e., on the “CO-annealed” surface (second sweep) the activity is significantly reduced because of the removal of surface defects in the presence of CO. As shown below, defect sites also play a role in CO ordering on platinum single-crystal surfaces.

The first *in-situ* determination of CO_{ad} structure was reported for a CO adlayer on Pt(111) in acidic electrolytes. Using *in-situ* STM, Villegas and Weaver [74, 78] observed a hexagonal close-packed (2×2) -3CO adlayer structure at potentials below 0.25 V (vs SCE), with a CO coverage of $\theta_{\text{CO}} = 0.75$ ML. The z-corrupted pattern evident in STM images indicated the presence of adsorbed CO at two threefold hollow Pt sites and one atop Pt site per (2×2) unit cell. At potentials above 0 V (up to the onset of CO oxidation), a markedly different adlayer arrangement was formed, having a $(\sqrt{19} \times \sqrt{19})R23.4^\circ$ -13CO unit cell with $\theta_{\text{CO}} = 13/19$. Following these earlier STM studies, direct information regarding the CO_{ad} structure was obtained in SXS measurements. While holding the potential at 0.05 V and with a continuous supply of CO to the X-ray cell, a diffraction pattern consistent with $p(2 \times 2)$ symmetry was observed, first by us [37, 71] and later by the Argonne [79] and Brookhaven [36] groups. Once formed, the

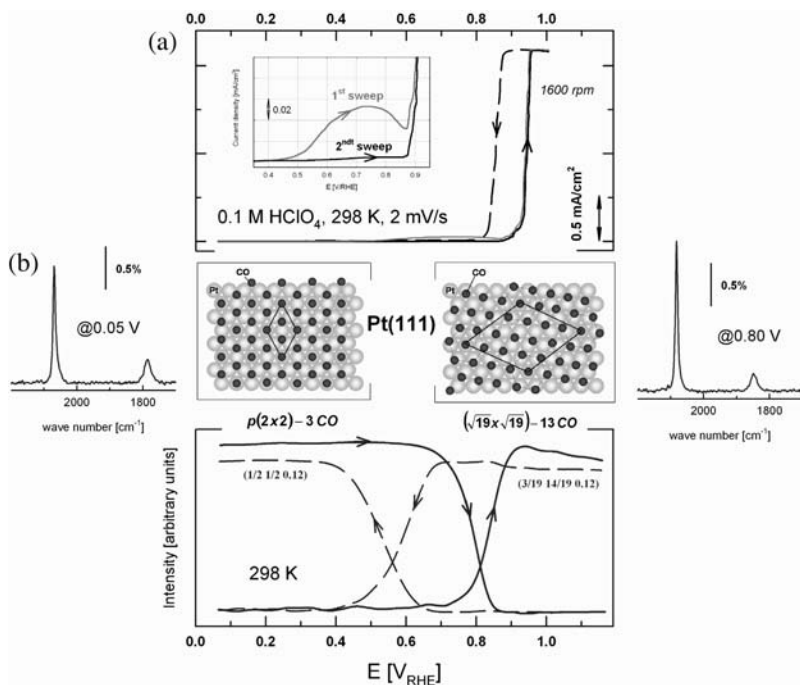


Fig. 1.15 (a) The polarization curve for CO oxidation on Pt(111) in CO-saturated 0.1 M HClO_4 solution at 298 K (sweep rate 2 mV/s). (b) A close-up of the pre-oxidation potential region showing the first and second anodic sweeps. (c) X-ray voltammetry measured at the $(\frac{1}{2}, \frac{1}{2}, 0.12)$ and

$(\frac{3}{19}, \frac{14}{19}, 0.12)$ positions where X-ray scattering arises due to the $p(2 \times 2)$ -3CO and $(\sqrt{19} \times \sqrt{19})$ -13CO structures respectively. Schematics of the CO structures, indicating the unit cells, are shown in between the two panels (unpublished data).

structure was stable only when the CO was continuously supplied to the X-ray cell, i.e., when CO was replaced by nitrogen the $p(2 \times 2)$ structure slowly vanished. It is also worth mentioning that the potential range of stability of the $p(2 \times 2)$ -3CO phase was strongly affected by the oxidation of a *small* fraction ($\sim 15\%$) of CO in the pre-ignition potential region. The potential window of stability as well as the domain size of this structure can be controlled by the nature of the anions present in supporting electrolytes. For example, in one study the CO coherent domain size increased from KOH (ca. 30 Å), to HClO_4 (ca. 140 Å), to $\text{HClO}_4^+\text{Br}^-$ (ca. 350 Å) electrolytes. Given that the potential range of stability increased in the same order, it was suggested [77] that CO ordering at low overpotentials is determined by the competition between OH_{ad} and spectator anions for the defect/step sites, i.e., the less active the surface is toward CO oxidation the larger the ordered domains and the greater the potential range of stability of the $p(2 \times 2)$ structure.

Fig. 1.15a shows that the disappearance of the $p(2 \times 2)$ -3CO structure at 0.7 V is accompanied by formation of the “ $\sqrt{19}$ ” structure, which is stable even in the

ignition potential region. This is a unique example of an adsorbate structure being present at a potential where maximum catalytic activity for an electrochemical reaction is observed. The observation of the " $\sqrt{19}$ " structure by SXS was reported first by Tolmachev et al. [79] in solution containing strongly adsorbing Br anions, and then by Wang et al. in perchloric acid solution [36]. The derived structural models for both the $p(2 \times 2)$ and " $\sqrt{19}$ " structures reveal that, while the $p(2 \times 2)$ structure consists of three CO molecules per unit cell, the unit cell of the " $\sqrt{19}$ " structure contains 13 CO molecules, thereby having a coverage, θ_{CO} , of 13/19 ($\theta_{\text{CO}} = 0.685$ per surface Pt atom). The *potential-induced* $p(2 \times 2) \leftrightarrow \sqrt{19}$ phase transition, discovered by Villegas and Weaver using STM experiments, has thus been confirmed by SXS results. Considering that under practical conditions in fuel cells the electrooxidation of impure hydrogen (i.e. containing a trace of CO) may take place over the temperature range 273–363 K, an intriguing question to answer is how the solution temperature affects the phase transitions in the CO structure. Temperature effects have long been studied in traditional (UHV-based) surface science, but, until recently, there had been no such attempts in interfacial electrochemistry. New results describing the effect of temperature on the $p(2 \times 2) \leftrightarrow \sqrt{19}$ phase transition in the CO adlayer on Pt(111) are presented below.

As in earlier studies at room temperature, the *temperature-controlled* $p(2 \times 2) \leftrightarrow \sqrt{19}$ phase transition (depicted in Fig. 1.16) was monitored by measuring the scattered X-ray intensities at $(1/2, 1/2, 0.12)$ and $(3/19, 14/19, 0.12)$ at 280 K, 293 K and 319 K for the same conditions as in Fig. 1.15. These results yield two significant new pieces of information that give new insight into the interaction of CO with OH on the Pt(111) surface.

1. The ordering of the $p(2 \times 2)$ -3CO structure is frustrated under both "cold" (280 K) as well as "hot" (319 K) conditions. The fact that the integrated intensities and the widths (inversely related to coherent domain size) of the $p(2 \times 2)$ peaks show a "volcano" relationship with the temperature of electrolyte may indicate that the balance between the rate of CO ordering and the surface coverage by OH (rate of CO oxidation) reaches a maximum at room temperature (293 K). Note also that the potential window of stability of the $p(2 \times 2)$ structure, shown in the middle part of Fig. 1.16, decreases linearly on increasing the temperature, reflecting the negative shift in the onset of CO oxidation on increasing temperature (observed in a top part of Fig. 1.16).
2. The ordering of the $\sqrt{19}$ structure (i.e. coherent domain size) increases linearly on increasing the temperature, a consequence of enhanced OH adsorption at high temperatures. It is also interesting that at 319 K the $\sqrt{19}$ phase exists even at the onset of the hydrogen evolution reaction (as shown in the bottom part of Fig. 1.16 at ca. 0 V). It is important to note that in the potential range where CO oxidation depends entirely on the rate of CO diffusion from the bulk of the solution to the Pt surface, the $\sqrt{19}$ structure is rather stable. This, in turn, suggests that the surface coverage by CO, in the potential region where diffusion limiting currents for CO oxidation are observed, is rather high (0.68 ML), a rather surprising result (!). The results presented in the fol-

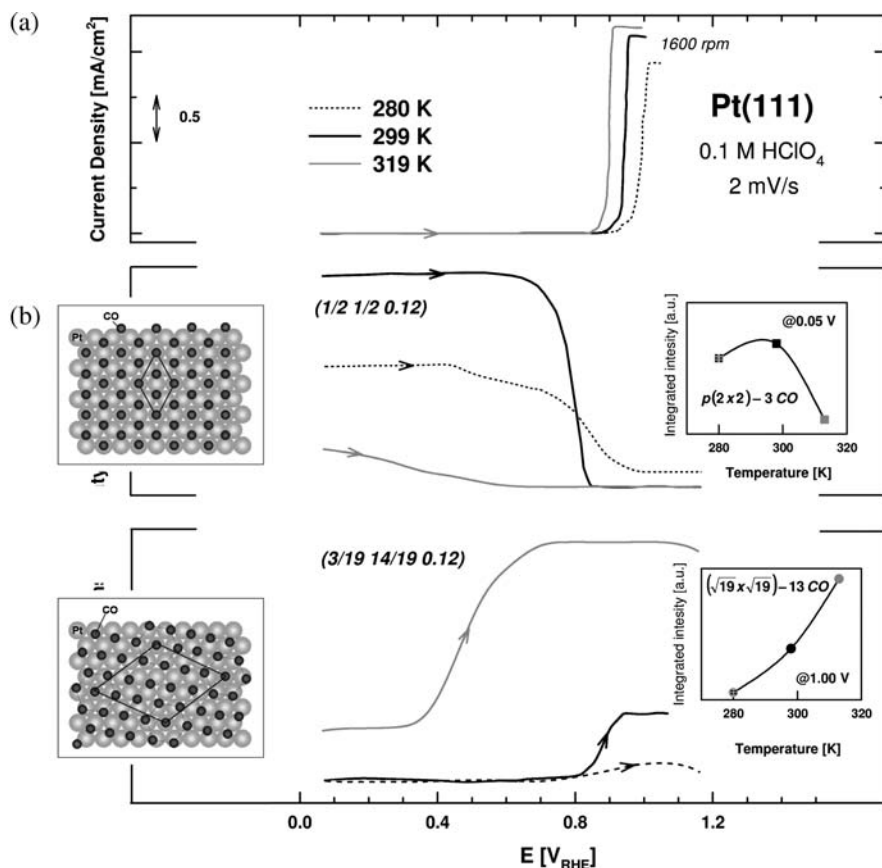


Fig. 1.16 (a) Polarization curves for CO oxidation for Pt(111) in CO-saturated 0.1 M HClO₄ solution measured at temperatures of 280 K (dotted line), 299 K (black line) and 319 K (grey line) (sweep rate 2 mV s⁻¹). Only the anodic sweeps are shown. (b) The corresponding XRVs measured at $(\frac{1}{2}, \frac{1}{2}, 0.12)$

and $(\frac{3}{19}, \frac{14}{19}, 0.12)$. The same color convention is used. The insets show the integrated intensities at the two positions as a function of the temperature, measured at 0.05 V and 1.0 V for the $p(2 \times 2)-3\text{CO}$ and $(\sqrt{19} \times \sqrt{19})-13\text{CO}$ structures respectively (unpublished results).

lowing section further demonstrate the richness of CO surface electrochemistry in a variety of metal-adsorbate systems.

1.4.3

Underpotential Deposition (UPD)

Metal UPD corresponds to the electrochemical adsorption, often of one monolayer, that occurs at electrode potentials positive with respect to the Nernst potential below which bulk metal adsorption occurs [80]. Numerous experiments have shown that the UPD layer can dramatically alter the chemical and elec-

tronic properties of the interface. The UPD layer is also the first stage of bulk metal deposition, and its structure can therefore strongly influence the structure of the bulk deposit. UPD was the first process to be studied using synchrotron X-ray diffraction in the late 1980s [1]. Quite a few systems have now been studied using this technique, and this has led to a greater understanding of the physics determining the structure of the UPD layer, in particular with regard to the role of the electrode potential and of various other adsorbing species that can be present in solution. In fact, considerable work was devoted to the co-adsorbate structures formed during UPD in the presence of halide anions, and results for Pt(*hkl*) and Au(*hkl*) surfaces have recently been reviewed [29].

To illustrate the complexity of structural behavior that can be observed in such systems, Fig. 1.17 summarizes X-ray diffraction results obtained during the UPD of Tl onto Au(111) in the presence of bromide anions [81, 82]. The top panel shows the cyclic voltammetry for Au(111) in 0.1 M HClO₄ containing 1 mM TlBr along with schematic models of the structures that were observed in

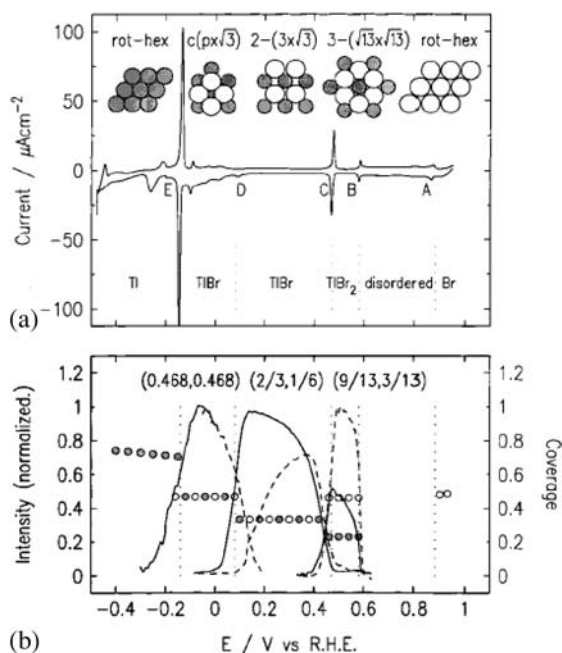


Fig. 1.17 (a) Voltammetry curve for the UPD of Tl on Au(111) in 0.1 M HClO₄ containing 1 mM TlBr. Sweep rate 20 mV s⁻¹. The in-plane and surface normal structural models are deduced from the SXS measurements. (b) Potential-dependent diffraction intensities at the indicated positions for the three coadsorbed phases. Scan rate

0.5 mV s⁻¹, except for the c(2.14×3) phase at (0.468, 0.468), where it is 0.2 mV s⁻¹, started after holding the potential around -0.1 V for several hours. Coverages, in units of monolayers of the Au substrate, shown by the open and filled circles for Br and Tl, respectively, are calculated from the adlayer lattice constants (taken from Refs. [81, 82]).

each potential range. The voltammetry shows many peaks that are not observed in the absence of bromide, and these peaks can be attributed to the coadsorption of bromide during Tl UPD. In the potential region on the positive side of peak A, bromide forms the rotated-hexagonal, close-packed adlayer, as observed in solution free of Tl. Similarly in the potential region on the negative side of peak E, thallium forms a rotated-hexagonal, close-packed monolayer that is also observed in solution free of bromide. At intermediate potentials, however, three superlattice structures consisting of mixed TlBr adlayers were observed. The lower part of Fig. 1.17 shows the measured X-ray intensity at the superlattice reciprocal lattice positions corresponding to each structure as a function of the applied potential and also the bromide and thallium coverage. The fact that the $(\sqrt{13} \times \sqrt{13})$ and $(3 \times \sqrt{3})$ structures are commensurate with the Au lattice highlights the importance of the substrate-adlayer bond, although the composition of the adlayers is best understood in terms of surface compound formation. Similar results were also observed for Tl-I, T-Cl and Pb-Br compounds formed on Au(111) [83].

In contrast to the Tl-halide systems, the structures formed during the UPD of Cu onto Au(*hkl*) and Pt(*hkl*) in the presence of halide (or sulfate) anions are dictated by the anion structures. For example, on Pt(111), Cu UPD in the presence of bromide is a two-stage process in which the hexagonal anion adlayer remains on the surface, causing an incommensurate CuBr bilayer to be formed at intermediate potentials (a structure that can accommodate a range of Cu coverage) until the Cu monolayer is formed at lower potentials prior to bulk Cu deposition [84]. Similarly, on Pt(100), formation of the Cu UPD monolayer leads to ordering of the bromide adlayer into a $c(2 \times 2)$ structure because of the strength of the Cu-Br bond [85]. The Cu-Br interaction can be considered to be cooperative in nature compared to the Pb-Br interaction, in which the Pb and Br adatoms compete for the Pt surface sites [86]. For example, on the Pt(100) surface this competition causes a negative shift in the electrode potential for the formation of the Pb $c(2 \times 2)$ structure and prevents the completion of the Pb monolayer as Br remains adsorbed on the Pt surface [87].

In determining the electrochemical reactivity of a surface toward a particular chemical reaction, it is clear that the electrode potential is key in determining the relative coverage by anion and/or cation species. For example, the coverage by anion species is an important factor in determining the rate of the oxygen reduction reaction on transition metal surfaces [29]. It is also important, however, to remember that the electrochemical interface is in chemical equilibrium and that adsorption/desorption processes are determined by the energies of adsorption unless kinetic barriers are present. This latter effect was illustrated in recent studies of the adsorption and oxidation of CO on Pt(*hkl*) surfaces modified by UPD metals. In these studies, RRDE and SXS measurements showed that UPD Cu and Pb are almost completely displaced from the Pt(100) and Pt(111) surfaces in perchloric acid (free of halide anions) by CO [14, 15]. Although these results are somewhat surprising and would not be observed in UHV studies, metal displacement can be understood from a simple thermodynamic analy-

sis by calculating the Gibbs energy change (ΔG) for the component steps of the process [88]. These calculations predict the spontaneous displacement of Cu and Pb by CO from the Pt electrode due to the corresponding exothermicity of the overall ΔG .

For the Pb/Pt(111) system, some insight into the displacement mechanism was obtained by studying the temporal evolution of the Pb- $(3 \times \sqrt{3})$ structure as CO was introduced to the solution. The inset to Fig. 1.18a shows a rocking scan through the $(4/6, 1/6, 0.2)$ position, where scattering from the $(3 \times \sqrt{3})$ structure occurs. The solid line is a Lorentzian fit to the line shape which enables a coherent domain size of ca. 160 Å to be calculated for this structure. The main part of Fig. 1.18a shows the time dependence of the peak intensity after CO was introduced to the solution at $\tau \approx 200$ s. The presence of CO in solution initially caused a large increase in the intensity due to the $(3 \times \sqrt{3})$ phase. This could be due to displacement of Pb that is adsorbed on the Pt surface in defect

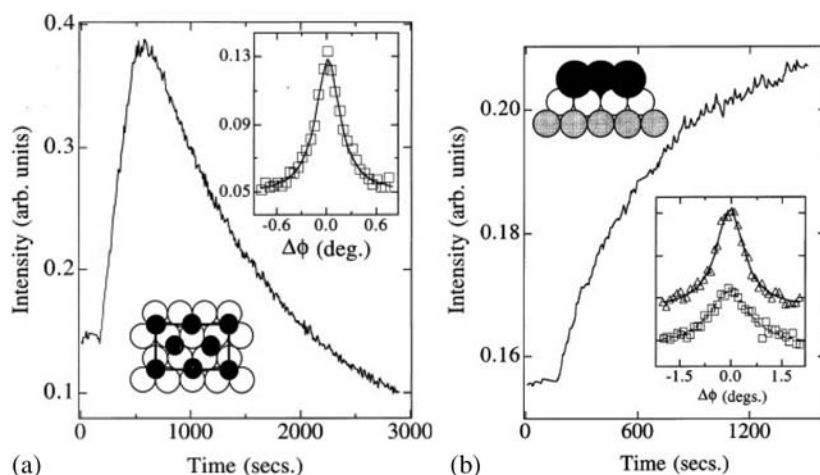


Fig. 1.18 (a) Time dependence of the X-ray scattering intensity at $(4/6, 1/6, 0.1)$, a Bragg reflection due to the $(3 \times \sqrt{3})$ -Pb structure on Pt(111). CO was introduced to the solution at $\tau \approx 200$ sec. Inset is a rocking curve measured at $(4/6, 1/6, 0.1)$ at the beginning of the experiment. The $(3 \times \sqrt{3})$ unit cell is illustrated schematically in the figure, where the open circles are surface Pt atoms and the filled circles are Pb adatoms. The Pb adlayer is uniaxially compressed relative to a hexagonal phase. (b) Time dependence of the X-ray scattering intensity at $(1/2, 1/2, 0.1)$, a Bragg reflection due to a $c(2 \times 2)$ Br adlayer on a $p(1 \times 1)$ Cu monolayer on Pt(100). CO was introduced to the solution

at $\tau \approx 200$ s. Inset are two rocking scans through the $(1/2, 1/2, 0.1)$ position (the data are displaced for clarity); squares represent data measured at the beginning of the experiment and triangles after the intensity level had reached an equilibrium value after the introduction of CO. The fitted Lorentzian line shape indicate an increase in domain size from ~ 50 Å to ~ 70 Å and a 25% increase in the integrated intensity. A side view of the structure is shown schematically, where the Cu forms a pseudomorphic monolayer on the Pt surface and the Br atoms are in the $c(2 \times 2)$ symmetry (taken from Ref. [29]).

sites, i.e., sites that are not commensurate with the $(3\times\sqrt{3})$ phase. The displaced Pb is incorporated into the $(3\times\sqrt{3})$ structure because of its increased mobility on the Pt surface, and thus the surface is populated by segregated domains of CO and the $(3\times\sqrt{3})$ Pb structure. This interpretation is supported by two additional X-ray measurements, performed when the intensity in Fig. 1.18a had reached the maximum value. Firstly, a rocking curve through the $(4/6, 1.6, 0.2)$ reflection indicated an increase in integrated intensity by a factor of three and an increase in domain size to ca. 200 Å. Secondly, a rocking curve at $(0, 1, 0.5)$, a position which is sensitive to the Pb coverage, indicated that the surface coverage by Pb had been reduced by ca. $10\pm 5\%$, i.e., only a small fraction of the Pb monolayer had been displaced by CO. Initially, displacement of Pb by CO causes increased ordering in the $(3\times\sqrt{3})$ structure. Presumably the Pb atoms initially displaced are “extra” atoms not in the $(3\times\sqrt{3})$ domains, probably at the domain boundaries. Replacement of some of the Pb atoms by CO (a smaller molecule) appears to allow additional ordering of the remaining atoms. The nature of the Pb-CO interaction is, however, repulsive. Given that there is also a repulsive Pb-Pb interaction in the $(3\times\sqrt{3})$ adlayer due to the uniaxial compression which decreases the Pb-Pb interatomic spacing [89], it is apparent that the repulsive forces weaken the Pt-Pb bond, which creates a kinetic pathway for the displacement [90]. Pb in the $(3\times\sqrt{3})$ phase is then displaced from the surface by CO, and the intensity of the $(3\times\sqrt{3})$ peak decreases until, at $\tau \approx 3000$ s, it has almost disappeared.

The effect of halide anions on the CO-metal displacement process can be dramatic. For the Cu-Br/Pt(100) system, the inset of Fig. 1.18b shows rocking curves through $(1/2, 1/2, 0.1)$, i.e. the strongest $c(2\times 2)$ reflection, in the case of the open squares for the structure formed in solution free of CO. The Lorentzian line shape (dashed line) indicates a domain size in the region of ca. 50 Å. The intensity was then monitored at this position as CO was introduced to the X-ray cell (similarly to Fig. 1.18a). Surprisingly, CO appears to enhance the $c(2\times 2)$ structure, and the rocking curve shown by triangular symbols in the inset to Fig. 1.18b was measured when the intensity at $(1/2, 1/2, 0.1)$ had reached a stable level. The fit to this peak gives a domain size of ca. 70 Å and also indicates an approximately 25% increase in integrated intensity. It appears, therefore, that bromide in solution prevents the complete displacement of UPD Cu that was observed in Br-free solution. In addition, coadsorption of CO appears to enhance the ordering in the $c(2\times 2)$ structure. At this point it is likely that the surface contains segregated domains of CO and the Cu-Br $c(2\times 2)$ structure. Cycling the potential anodically lifted the Cu-Br structure, and the surface became fully populated by CO. Once this had occurred, the UPD process was completely blocked, and the surface remained covered by CO over the whole potential range during cycling (see [15] for more details). For the Pb-Br system, the Pb $c(2\times 2)$ structure was formed at 0.0 V before CO was introduced to the X-ray cell. In this case the scattering at $(1/2, 1/2, 0.1)$ disappeared immediately and XRV measurements indicated that CO had completely displaced Pb and Br from the surface as potential cycling caused no change in the measured X-ray

intensity. It appears, therefore, that because Pb and Br are competing for the Pt surface adsorption sites, which presumably weakens the bonds between the adsorbing species and the substrate, CO displaces the Pb-Br adlayer, i.e., there is no energetic barrier to displacement, as suggested for the Cu-Br system. Almost identical effects were observed for the Pt(111) surface, i.e., CuBr blocked CO adsorption prior to potential cycling whereas PbBr was completely displaced and the ordered $p(2 \times 2)$ -3CO structure was formed. These results show that the nature of the metal-anion interaction, and hence the strength of the adlayer-Pt bond, is crucial in determining the interaction with solution CO.

The goal of linking surface atomic structure to reactivity is shared by the UHV heterogeneous catalysis community. The above results, however, highlight some clear differences between these two research areas that must be considered if common themes are to emerge. In particular, modification of an electrode surface by a UPD metal monolayer is not always equivalent to the UHV deposition counterpart, as the energetics of adatoms can be very different at the solid/liquid interface. This is clearly illustrated by the phenomenon of surface displacement, which cannot be observed under non-equilibrium UHV conditions.

1.5

Reactive Metals and Oxides

So far in this article we have focused on the surface structures observed on Pt, Pt-based alloys, and Au single-crystal electrodes. A key quality that has emerged from these studies is that the surfaces are stable, provided that the applied potential is restricted to a certain range remote from irreversible reactions such as oxide formation [91]. Experimentally, this is advantageous, in that detailed SXS measurements from a particular system can be obtained in a time scale over which the surface undergoes no structural modification. More reactive metal surfaces present a greater challenge because of the problems associated with the transfer of a prepared crystal into the X-ray electrochemical cell and the stability of the surface in the electrochemical environment. Of course, the structure and growth of passive films on metal electrodes has been an extensively studied subject because of the influence on corrosion properties of materials. In this section, we briefly review SXS measurements of passive film formation on reactive metal surfaces and then finally describe some recent measurements of a material with widespread technological application, namely ruthenium oxide.

The structure of the passive oxide film formed on iron has been the subject of much controversy dating back to the discovery of the phenomenon in the 1700s because of the difficulty in characterizing the thin film in the aqueous environment, and it is only recently that SXS has been able to resolve some of the issues. M. F. Toney and co-workers [92] used SXS to study the passive oxide films formed on single-crystal Fe(001) and Fe(110) substrates at a high anodic formation potential. Fig. 19 a and b show the measured diffraction patterns from the passive film on Fe(001) and Fe(110) respectively. For growth on Fe(001), the oxide (001) planes

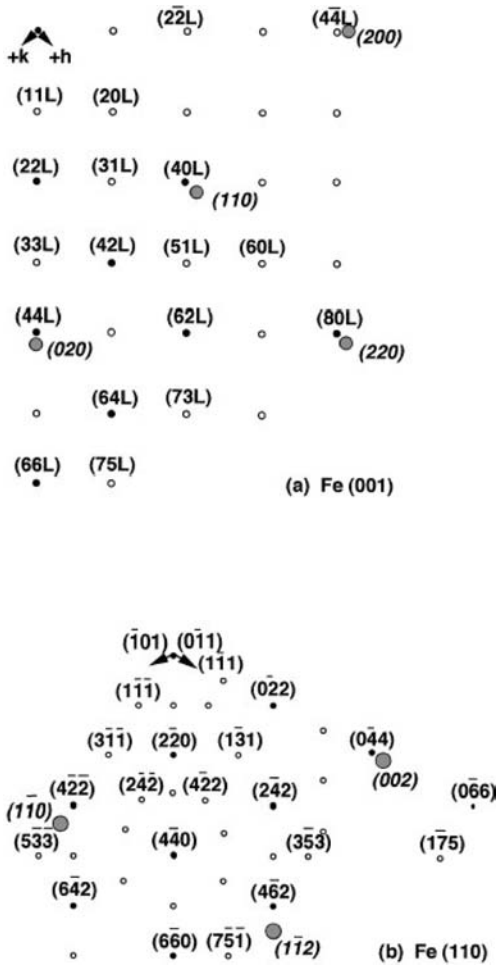


Fig. 1.19 One quadrant of the diffraction pattern for the passive film on (a) Fe(001) and (b) Fe(110). For clarity only some of the out-of-plane peaks are shown. In (a) these are collectively denoted by L. The diffraction peaks from the oxide are represented by

small filled and open circles (which are purely in-plane peaks and peaks that are nearly in plane, respectively). Substrate peaks are represented by the large, lightly shaded circles (taken from Ref. [92]).

lie parallel to the Fe surface, while for Fe(110) the oxide (111) planes are parallel to the surface. For both surfaces the oxide $[-1\ 1\ 0]$ direction is parallel to Fe[100]. Qualitatively, the diffraction patterns are consistent with those of spinel oxides ($\gamma\text{Fe}_2\text{O}_3$, Fe_3O_4 , or related structures). The detailed atomic structure, however, was deduced by modeling of the structure factors of 68 symmetry-inequivalent diffraction peaks, and a comparison of the measured and best-fit structure factors for a subset of these peaks is shown in Fig. 1.20. The calculated structure factors for

the Fe_3O_4 and $\gamma\text{Fe}_2\text{O}_3$ structures are shown by open square symbols and open circle symbols respectively, and the clear disagreement with some of the measured structure factors establishes that they are not present in the passive film. The filled diamonds give the best agreement with the measured data, the so-called LAMM structure that is based on a spinel oxide structure with random cation vacancies and interstitials (see [92] and [93]). Determination of the LAMM passive film structure resolves many of the discrepancies in interpretations of experimental data based on other structural models and highlights the applicability and strength of the *in-situ* SXS technique in the study of oxide films.

The formation of passive oxide films on the (111) surfaces of Cu and Ni has also been studied in detail by SXS [94, 95]. Measurements of Cu(111) in 0.1 M NaClO_4 (at pH 4.5) showed that the oxide exhibited a crystalline cuprite structure (Cu_2O) that was epitaxially aligned with the underlying Cu substrate [94]. Although a similar oxide structure was observed for oxidation in air, there were some key differences in the structure of the aqueous oxide. In particular it was found that a preferred “reversed” orientation of the oxide film was formed, and this indicated that oxide growth occurs at the interface between the oxide and the Cu(111) surface

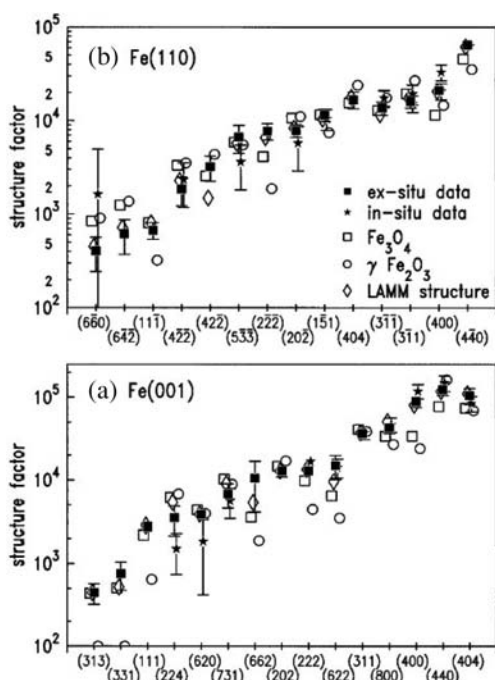


Fig. 1.20 Measured and best-fit structure factors for a subset of the diffraction peaks for the passive film grown on (a) Fe(001) and (b) Fe(110). Measured data are shown by black-filled squares. The best fits for the

model structures are open squares for Fe_3O_4 , open circles for $\gamma\text{Fe}_2\text{O}_3$, and filled diamonds for the LAMM phase (taken from Ref. [93]).

rather than at the oxide/electrolyte interface. The passive oxide film formed on an Ni(111) electrode in sulfuric acid electrolyte consisted of a duplex structure with a crystalline inner NiO(111) layer and a porous, amorphous hydroxide phase at the interface between the NiO surface and the electrolyte [96]. Similarly to Cu(111), there were differences between the air-formed and aqueous oxides, although in the case of Ni the air-formed oxide underwent a slow conversion to the aqueous oxide following immersion in electrolyte. The existence of the duplex oxide structure is key in understanding the behavior of the Ni electrode in alkaline solution. In this case a combined SXS/AFM study revealed that cycling the electrode potential over the $\text{Ni(OH)}_2/\text{NiOOH}$ redox peaks led to an increase in thickness of both the compact NiO layer and the amorphous hydroxide phase [97]. The thickening of the dense NiO phase limits further growth of the hydroxide phase, because of either limited Ni diffusion from the Ni substrate or the reduction in potential gradient across the NiO film.

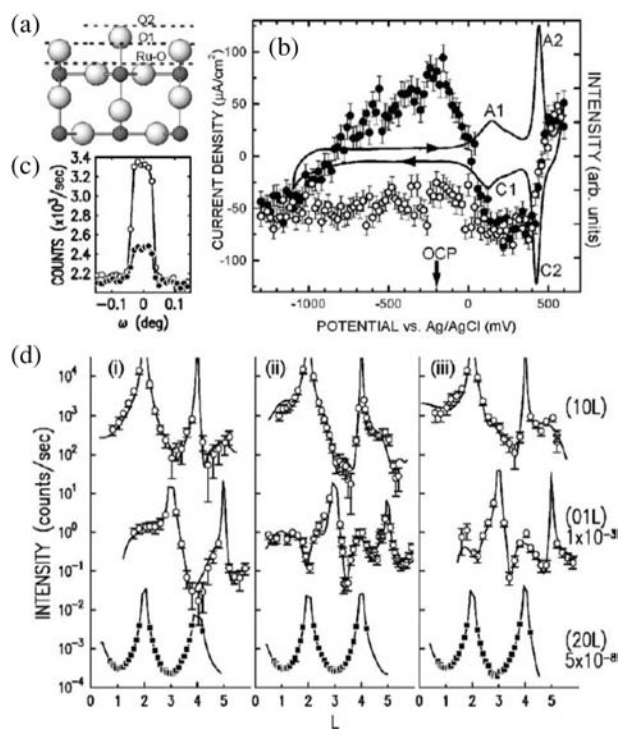


Fig. 1.21 (a) Possible three terminations of RuO₂ structure discussed in Ref. [99]. (b) Cyclic voltammogram (solid line) for the RuO₂(110) surface in 0.1 M NaOH. The arrows indicate the sweep directions. Solid and open circles are the X-ray intensity measured at (0, 1, 4) during cathodic and

anodic sweeps respectively. (c) ω scans at (014) (d) (1, 0, L) and (0, 1, L) "oxygen rods" and the (2, 0, L) CTR measured at (i) 330 mV, (ii) 500 mV and (iii) -200 mV. The solid lines are fits to the data according to the structural models shown in Fig. 1.22 (taken from Ref. [99]).

Conducting metal oxides are of widespread technological importance in electrochemistry, and their study by synchrotron SXS has recently been described in a review of the mineral/water interface [98]. Ruthenium dioxide is of particular interest from the catalytic point of view, partly because Ru is an important material in Pt-Ru electrocatalysts for fuel cell applications, but also because RuO_2 is routinely used in industrial electrolysis for chlorine, oxygen, and hydrogen production. H. You and co-workers have carried out a series of SXS experiments on well-defined RuO_2 single-crystal surfaces [99–101], and some of the key results are summarized in Fig. 1.21 for the $\text{RuO}_2(110)$ electrode in 0.1 M NaOH electrolyte. Fig. 1.21b shows the cyclic voltammetry which displays two distinct reversible reactions at electrode potentials of ca. 150 mV and 400 mV. Also shown is the X-ray scattering signal measured at (1, 0, 4) for the cathodic (solid circles) and anodic (open circles) sweeps. These data indicate that structural changes are associated with both of the peaks in the CV, the reaction at ca. 150 mV showing considerable hysteresis. The XRV measurements define three electrode potentials for potentiostatic CTR measurements, and these data are shown in Fig. 1.21b. A particularly advantageous feature of the CTR data is that, for the $\text{RuO}_2(110)$ bulk structure, the scattering contribution from the two Ru sublattices vanishes when $H + K$ is odd, and so for these CTRs the scattering is due only to the oxygen atoms. These so-called “oxygen rods” are thus extremely sensitive to commensurate surface oxygen, i.e. commensurate water,

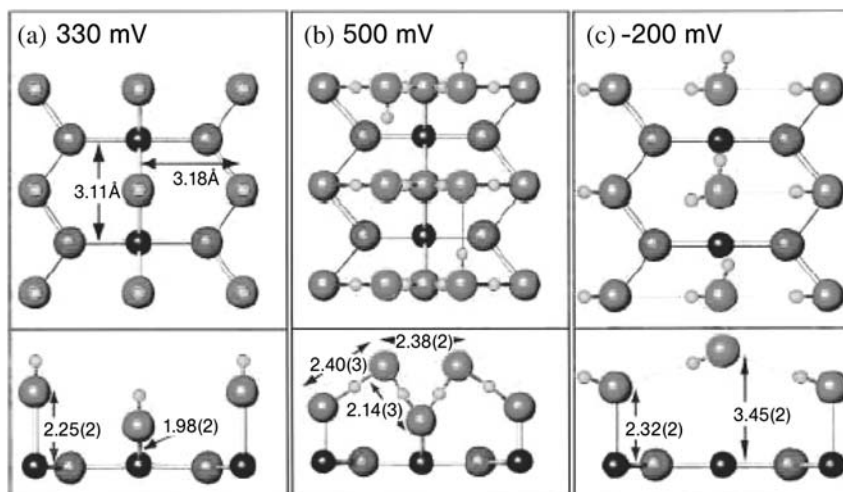


Fig. 1.22 Derived structural models of the $\text{RuO}_2(110)$ surface at the potentials corresponding to the data shown in Fig. 1.21b. The black balls represent the Ru atoms. The grey balls represent oxygen atoms in the bulk, on the surface bonded to Ru, and in the water molecules, respectively.

The small light grey balls represent the hydrogen atoms, conjectured to show conceivable hydrogen bonds. Horizontal direction: (010) $[(1-10)_{\text{bulk}}]$. Vertical direction: (100) $[(001)_{\text{bulk}}]$ for upper panels (top views); (001) $[(110)_{\text{bulk}}]$ for lower panels (side views) (taken from Ref. [99]).

and this enabled a detailed modeling of the water structure at the interface [99]. It should be noted that previous attempts at identifying the water structure at the charged electrochemical interface have been somewhat controversial (as mentioned in Section 1.3.1.2) because of the relative weakness of the scattering from the water layers compared to the underlying metal substrate [44]. Although the (2, 0, L) CTR is relatively unchanged at the three electrode potentials, the “oxygen rods” show dramatic changes. Analysis of the CTR data led to the structural models for the surface terminations shown in Fig. 1.22. These models indicate that, at potentials close to oxygen evolution (500 mV), a layer of water molecules is vertically compressed to the surface oxygen layer by the strong electric field and that the formation of these layers may be a precursor to oxygen evolution. As the potential decreases, the bilayer converts to a simple OH layer bonded to Ru atoms (330 mV) and then to a layer of commensurate water stabilized by an O...H–O hydrogen network anchored to atop OH molecules (–200 mV).

1.6

Conclusions and Future Directions

It is apparent that during approximately the last 15 years a great deal has been learned from the application of SXS techniques to the study of the electrode/solution interface. Particular (but not exclusive) examples include (a) surface reconstruction and relaxation phenomena, (b) understanding the potential dependence of surface structures, (c) correlations that have been established between surface expansion and the energetics of adsorption, the pzc and its relation to structural properties, etc., (d) the extension of the potential range from H_{upd} to H_{opd} to learn about hydrogen absorption effects, (e) the fact that CO adsorption can lead to some surprising effects in electrochemistry, such as the enhancement of surface reconstruction and the displacement of adsorbed metal layers, (f) the *in-situ* monitoring of active surface sites during electrochemical reactions, and (g) studies of bulk metal deposition, corrosion, and conducting metal oxides.

As the emphasis of surface science studies using synchrotron radiation continues to shift away from the UHV characterization of surface structures to explore the relationship between structure and functionality, the electrochemical interface will continue to be at the forefront of such research. We envisage a number of areas that are ripe for investigation.

1. The study of temperature effects (see Section 1.4.2), which has already begun, should continue to explore both the possible existence of temperature-induced phase transitions and surface stability issues in materials of technological importance.
2. There should be increased study of bimetallic surfaces to establish structural trends in surface behavior across the periodic table and the correlation between these trends and electrocatalytic reactivity.

3. Further studies of semiconductor materials relevant to the development of photo-voltaic devices.
4. A better understanding of the electronic properties of selected surface atoms probed via resonant X-ray diffraction techniques.

Finally, we hope that the success of the collaboration between electrochemists and the SXS community can be extended to other interdisciplinary research areas, such as bioelectrochemistry.

Acknowledgments

This work was supported by the Director, Office of Science, Office of Basic Energy Sciences, Division of Materials Sciences, U.S. Department of Energy under Contract No. DE-AC03-76SF00098. CAL would like to acknowledge the support of an EPSRC Advanced Research Fellowship. Original data was measured at SSRL, which is funded by the Division of Chemical Sciences (DCS), US DOE, and the EPSRC-funded XMaS CRG beamline (BM28) at the ESRF, Grenoble. Other data is referenced in the figure captions. We would like to acknowledge the following people for their invaluable contributions to this work; Mathias Arenz, Matthew Ball, Berislav Blizanac, Ben Fowler, Mark Gallagher, Philip Ross, Vojislav Stamenkovic, and Paul Thompson.

References

- 1 M.G. Samant, M.F. Toney, G.L. Borges, K.F. Blurton, and L.M.O.R. Blum, *J. Phys. Chem.*, 92 (1988) 220.
- 2 B.M. Ocko, J. Wang, A. Davenport, and H. Isaacs, *Phys. Rev. Lett.*, 65 (1990) 1466–1469.
- 3 M.F. Toney and B.M. Ocko, *Synchrotron Radiation News*, 6 (1993) 28–33.
- 4 I.M. Tidswell, N.M. Markovic, and P.N. Ross, *Phys. Rev. Lett.*, 71 (1993) 1601–1604.
- 5 C. Lucas, N.M. Markovic, and P.N. Ross, *Surf. Sci.*, 340 (1996) L949–L954.
- 6 C. Lucas, N.M. Markovic, and P.N. Ross, *Phys. Rev. Lett.*, 77 (1996) 4922–4925.
- 7 D.M. Kolb, *Prog. Surf. Sci.*, 51 (1996) 109–173.
- 8 K. Itaya, *Prog. Surf. Sci.*, 58 (1998) 121–247.
- 9 I.M. Tidswell, N.M. Markovic, C. Lucas, and P.N. Ross, *Phys. Rev. B*, 47 (1993) 16542.
- 10 R. Feidenhans'l, *Surf. Sci. Rep.*, 10 (1989) 105–188.
- 11 P.H. Fuoss and S. Brennan, *Annu. Rev. Mater. Sci.*, 20 (1990) 360.
- 12 I.K. Robinson and D.J. Tweet, *Rep. Prog. Phys.*, 55 (1992) 599.
- 13 I.K. Robinson, *Phys. Rev. B*, 33 (1986) 3830.
- 14 C.A. Lucas, N.M. Markovic, B.N. Grgur, and P.N. Ross Jr., *Surf. Sci.*, 448 (2000) 65–76.
- 15 C.A. Lucas, N.M. Markovic, and P.N. Ross Jr., *Surf. Sci.*, 448 (2000) 77–86.
- 16 J. Clavilier, *J. Electroanal. Chem.*, 107 (1980) 211–216.
- 17 N.M. Markovic, M. Hanson, G. McDougal, and E. Yeager, *J. Electroanal. Chem.*, 241 (1986) 309.
- 18 L.A. Kibler, M. Cuesta, M. Kleinert, and D.M. Kolb, *J. Electroanal. Chem.*, 484 (2000) 73–82.

- 19 M.G. Samant, M.F. Toney, G.L. Borges, L. Blum, and O.R. Merloy, *Surf. Sci.*, 193 (1988) L29.
- 20 Y.S. Chu, I.K. Robinson, and A.A. Gewirth, *Phys. Rev. B*, 55 (1997) 7945.
- 21 O.M. Magnussen, J. Scherer, B.M. Ocko, and R.J. Behm, *J. Phys. Chem.*, 104 (2000) 1222.
- 22 G.A. Somorjai and M.A. Van Hove, *Prog. Surf. Sci.*, 30 (1989) 201.
- 23 G.A. Somorjai, *Introduction to Surface Chemistry and Catalysis*, John Wiley & Sons, New York, 1993.
- 24 P.A. Thiel and P.J. Estrup, in A.T. Hubbard (Ed.), *The Handbook of Surface Imaging and Visualization*, CRC Press, Boca Raton, 1995.
- 25 R.I. Masel, *Principles of Adsorption and Reaction on Solid Surfaces*, John Wiley & Sons, Inc., 1996.
- 26 M.A. Van Hove, in Landolt-Börnstein (Ed.), *Physics of Covered Solid Surfaces*, 1999.
- 27 J. Greeley, J.K. Norskov, and M. Mavrikakis, *Annu. Rev. Phys. Chem.*, 53 (2002) 319–348.
- 28 N.M. Markovic and P.S. Ross, *Surf. Sci. Rep.*, 45 (2002) 117–230.
- 29 C.A. Lucas and N.M. Markovic, in Ernesto J. Calvo (Ed.), *The Encyclopedia of Electrochemistry*, Vol. 2, Section 4.1.2.1.2, Wiley-VCH, 2004.
- 30 V. Stamenkovic, M. Arenz, C. Lucas, M. Gallagher, P.N. Ross, and N.M. Markovic, *J. Am. Chem. Soc.*, 125 (2003) 2736–2745.
- 31 M.E. Gallagher, C.A. Lucas, V. Stamenkovic, N.M. Markovic, and P.N. Ross, *Surf. Sci.*, 544 (2003) L729–L734.
- 32 N.M. Markovic, C. Lucas, V. Climent, V. Stamenkovic, and P.N. Ross, *Surf. Sci.*, 465 (2000) 103–114.
- 33 M. Ball, C. Lucas, V. Stamenkovic, P.N. Ross, and N.M. Markovic, *Surf. Sci.*, 518 (2002) 201–209.
- 34 M. Ball, C.A. Lucas, N.M. Markovic, V. Stamenkovic and P.N. Ross, *Surf. Sci.*, 540 (2003) 295–302.
- 35 I.M. Tidswell, N.M. Markovic, and P.N. Ross, *J. Electroanal. Chem.*, 376 (1994) 119–126.
- 36 J. Wang, I.K. Robinson, B.M. Ocko, and R.R. Adzic, *J. Phys. Chem.*, 109 (2005) 24–26.
- 37 C.A. Lucas, N.M. Markovic, and P.N. Ross, *Surf. Sci.*, 425 (1999) L381–L386.
- 38 T.E. Shubina and M.T.M. Koper, *Electrochim. Acta*, 47 (2002) 3621–3628.
- 39 H. Naohara, S. Ye, and K. Uosaki, *J. Phys. Chem. B*, 102 (1998) 4366–4373.
- 40 G. Jerkiewicz, *Prog. Surf. Sci.*, 57 (1998) 137–186.
- 41 Y. Sung, W. Chrzanowski, A. Wieckowski, A. Zolfaghari, S. Blais, and G. Jerkiewicz, *Electrochim. Acta*, 44 (1998) 1019.
- 42 W. Haiss, R.J. Nichols, J. Sass, and K. Charle, *J. Electroanal. Chem.*, 452 (1998) 199.
- 43 R.J. Nichols, T. Nouar, C.A. Lucas, W. Haiss, and W.A. Hofer, *Surf. Sci.*, 263 (2002) 513.
- 44 M.F. Toney, J.N. Howard, J. Richer, G.L. Borges, J.G. Gordon, O.R. Merloy, D. Wiesler, D. Yee, and L.B. Sorensen, *Nature*, 368 (1994) 444.
- 45 S.Y. Chu (1997) PhD thesis, Department of Physics, University of Illinois.
- 46 M.E. Gallagher, C.A. Lucas, B.B. Blizanac, P.N. Ross, and N.M. Markovic, *Surf. Sci.*, to be submitted.
- 47 S.L. Horswell, A.L. Pinheiro, E. Savinova, B. Danckwerts, M.S. Zei, and G. Ertl, *Langmuir*, 20 (2004) 10970.
- 48 C.I. Carlisle, D.A. King, M.-L. Bockuet, J. Cerda, and P. Sautet, *Phys. Rev. Lett.*, 470 (2000) 15.
- 49 C.I. Carlisle, D.A. King, M.-L. Bockuet, J. Cerda, and P. Sautet, *Phys. Rev. Lett.*, 84 (2000) 3899.
- 50 J. Kunze, H.H. Strehblow, and G. Staiikov, *Electrochem. Comm.*, 6 (2004) 132.
- 51 K.M. Ho and K.P. Bohnen, *Phys. Rev. Lett.*, 59 (1987) 1833.
- 52 J.K. Norskov, *Surf. Sci.*, 299 (1994) 690.
- 53 J. Wang, J. Devenport, H. Isaacs, and B.M. Ocko, *Science*, 255 (1992) 1416–1418.
- 54 I.M. Tidswell, N.M. Markovic, and P.N. Ross, *Surf. Sci.*, 317 (1994) 241–252.
- 55 B.M. Ocko, B.C. Scharadt, and J. Wang, *Phys. Rev. Lett.*, 69 (1992) 3350–3353.
- 56 B.B. Blizanac, C. Lucas, M. Gallagher, M. Arenz, P.N. Ross, and N.M. Markovic, *J. Phys. Chem.*, 108 (2003) 625–634.

- 57 O.M. Magnussen, *Chem. Rev.*, 102 (2002) 679–725.
- 58 G. J. Edens, X. Gao, M. J. Weaver, N. M. Markovic, and P. N. Ross, *Surf. Sci. Lett.*, 302 (1994) L275–L282.
- 59 M. Gallagher, B. B. Blizanac, C. A. Lucas, P. N. Ross, and N. M. Markovic, *Surf. Sci.*, 582 (2005) 215–226.
- 60 B. B. Blizanac, C. A. Lucas, M. Gallagher, M. Arenz, P. N. Ross, and N. M. Markovic, *J. Phys. Chem.*, 108 (2004) 625–634.
- 61 B. M. Ocko, J. Wang, and T. Wandlowski, *Phys. Rev. Lett.*, 79 (1997) 1511.
- 62 D. W. Suggs and A. J. Bard, *J. Phys. Chem.*, 99 (1995) 8349.
- 63 C. M. Vitus, S. C. Chang, B. C. Schardt, and M. J. Weaver, *J. Phys. Chem.*, 95 (1991) 7559.
- 64 K. Sashikata, H. Matsui, K. Itaya, and M. P. Soriaga, *J. Chem. Phys.*, 100 (1996) 2027.
- 65 B. M. Ocko, O. M. Magnussen, J. X. Wang, and T. Wandlowski, *Phys. Rev. B*, 53 (2003) 7654–7657.
- 66 J. M. Gottfried, K. J. Schmidt, S. L. M. Schroeder, and K. Christmann, *Surf. Sci.*, 536 (2003) 206–224.
- 67 B. B. Blizanac, M. Arenz, P. N. Ross, and N. M. Markovic, *J. Am. Chem. Soc.*, 126 (2004) 10130–10141.
- 68 T. Wandlowski, J. X. Wang, O. M. Magnussen, and B. M. Ocko, *J. Phys. Chem.*, 100 (1996) 10277–10287.
- 69 R. J. Nichols, in J. Lipkowski and P. N. Ross (Eds.), *Adsorption of Molecules at Metal Electrodes*, VCH Inc., New York, 1992, Ch. 7.
- 70 C. Korzeniewski, in A. Wieckowski (Ed.), *Interfacial Electrochemistry – Theory, Experiment and Applications*, Marcel Dekker, Inc, New York, Basel, 1999, Ch. 20.
- 71 N. M. Markovic, B. N. Grgur, C. A. Lucas, and P. N. Ross, *J. Phys. Chem. B*, 103 (1999) 487–495.
- 72 N. P. Lebedeva, M. Koper, E. Herrero, J. M. Feliu, and R. A. van Santen, *J. Electroanal. Chem.*, 487 (2000) 37–44.
- 73 N. P. Lebedeva, A. Rodes, J. M. Feliu, M. T. M. Koper, and R. A. van Santen, *J. Phys. Chem. B*, 106 (2002) 9863–9872.
- 74 I. Villegas and M. J. Weaver, *J. Chem. Phys.*, 101 (1994) 1648.
- 75 K. Yoshima, M. Song, and M. Ito, *Surf. Sci.*, 368 (1996) 389.
- 76 N. M. Markovic, in W. Vielstich, A. Lamm, and H. A. Gasteiger (Eds.), *Handbook of Fuel Cells; Fundamentals, Technology and Application*, pp. 368–393, John Wiley & Sons Inc., 2003.
- 77 N. M. Markovic, C. A. Lucas, A. Rodes, V. Stamenkovic, and P. N. Ross, *Surf. Sci.*, 499 (2002) L149–L158.
- 78 I. Villegas, X. Gao, and M. J. Weaver, *Electrochim. Acta*, 40 (1995) 1267–1275.
- 79 Y. V. Tolmachev, A. Menzel, A. Tkachuk, S. Y. Chu, and H. You, *Electrochem. Solid-State Lett.*, 7 (2004) E23.
- 80 A. J. Bard and L. R. Faulkner, *Electrochemical Methods*, Wiley & Sons, New York, 1980.
- 81 R. R. Adzic and J. Wang, *J. Phys. Chem.*, 102 (1998) 6305.
- 82 J. Wang, I. K. Robinson, and R. R. Adzic, *Surf. Sci.*, 412/413 (1998) 374.
- 83 J. Wang, I. K. Robinson, J. E. DeVilbiss, and R. R. Adzic, *J. Phys. Chem. B*, 104 (2000) 7951.
- 84 N. M. Markovic, C. Lucas, H. A. Gasteiger, and P. N. Ross Jr., *Surf. Sci.*, 372 (1997) 239–254.
- 85 C. A. Lucas, N. M. Markovic, B. N. Grgur, and P. N. Ross, *Surf. Sci.*, 448 (1998) 65–76.
- 86 N. M. Markovic, B. N. Grgur, C. A. Lucas, and P. N. Ross, *J. Electroanal. Chem.*, 448 (1998) 183.
- 87 N. M. Markovic, B. N. Grgur, C. Lucas, and P. N. Ross, *J. Chem. Soc. Faraday Trans.*, 94 (1998) 3373–3379.
- 88 N. M. Markovic, B. N. Grgur, C. A. Lucas, and P. N. Ross Jr., *Langmuir*, 16 (2000) 1998–2005.
- 89 R. R. Adzic, J. Wang, C. M. Vitus, and B. M. Ocko, *Surf. Sci. Lett.*, 293 (1993) L876–L883.
- 90 J. M. White and S. Akhter, *Crit. Rev. Solid State Mater. Sci.*, CRC, 1988.
- 91 Z. Nagy and H. You, *Electrochim. Acta*, 47 (2005) 3037.
- 92 M. F. Toney, A. Devenport, M. P. Oblonsky, P. M. Ryan, and C. M. Vitus, *Phys. Rev. Lett.*, 79 (1997) 4282.
- 93 A. Davenport, M. P. Oblonsky, P. M. Ryan, and M. F. Toney, *J. Electrochem. Soc.*, 147 (2000) 2162.

- 94 S. Y. Chu, I. K. Robinson, and A. A. Gewirth, *J. Phys. Chem.*, 110 (1999) 5952.
- 95 J. Scherer, B. M. Ocko, and O. M. Magnussen, *Electrochim. Acta*, 48 (2003) 1169.
- 96 O. M. Magnussen, J. Scherer, B. M. Ocko, and R. J. Behm, *J. Phys. Chem.*, 104 (2000) 1222.
- 97 S. L. Medway, C. A. Lucas, A. Kowal, R. J. Nichols, and D. Johnson, *J. Electroanal. Chem.*, submitted for publication (2005).
- 98 P. Fenter and N. C. Sturchio, *Prog. Surf. Sci.*, 77 (2004) 171.
- 99 S. Y. Chu, T. E. Lister, W. G. Cullen, H. You, and Z. Nagy, *Phys. Rev. Lett.*, 86 (2001) 3364.
- 100 T. E. Lister, S. Y. Chu, W. G. Cullen, H. You, R. M. Yonco, J. F. Michell, and Z. Nagy, *J. Electroanal. Chem.*, 524/525 (2002) 201.
- 101 T. E. Lister, Y. V. Tolmachev, S. Y. Chu, W. G. Cullen, H. You, R. M. Yonco, and Z. Nagy, *J. Electroanal. Chem.*, 554/555 (2003) 71.
- 102 B. E. Conway, in S. Davison (Ed.), *Prog. Surf. Sci.*, Vol. 16, Pergamon Press, Fairview Park, NY, 1984.

